Mon. Not. R. Astron. Soc. **000**, 1–?? (2012) Printed 18 April 2013 (MN LaTeX style file v2.2)

arXiv:1304.4598v1 [astro-ph.CO] 16 Apr 2013

The VLT LBG Redshift Survey - IV. Gas and galaxies at $z \sim 3$ in observations and simulations

P. Tummuangpak[1]*, T. Shanks[1], R. M. Bielby[1], N. H. M. Crighton[2], H. Francke[3], L. Infante[3], T. Theuns[4,5]
[1] Department of Physics, University of Durham, South Road, Durham DH1 3LE, UK
[2] Max Planck Institute for Astronomy, Königstuhl 17, D-69117 Heidelberg, Germany
[3] Departamento de Astronomía y Astrofísica, Pontificia Universidad Catolica de Chile, Casilla 306, Santiago 22, Chile
[4] Institute for Computational Cosmology, Department of Physics, University of Durham, South Road, Durham, DH1 3LE, UK
[5] Department of Physics, University of Antwerp, Campus Groenenborger, Groenenborgerlaan 171, B-2020 Antwerp, Belgium

ABSTRACT

We use a combination of observations and simulations to study the relationship between star-forming galaxies and the intergalactic medium at $z \approx 3$. The observed star-forming galaxy sample is based on spectroscopic redshift data taken from a combination of the VLT LBG Redshift Survey (VLRS) data and Keck LRIS observations in fields centred on bright background QSOs, whilst the simulation data is taken from the GIMIC simulation. In the simulations, we find that the dominant peculiar velocities are in the form of large-scale coherent motions of gas and galaxies. Gravitational infall of galaxies towards one another is also seen, consistent with expectations from linear theory. At smaller scales, the rms peculiar velocities in the simulation overpredict the difference between the simulated real- and z-space galaxy correlation functions. Peculiar velocity pairs with separations smaller than 1 h^{-1}Mpc have a smaller dispersion and explain the z-space correlation function better. The Lyα auto- and cross-correlation functions in the GIMIC simulations, appear to show infall smaller than implied by the expected $\beta_{Ly\alpha} \approx 1.3$ (McDonald et al.). There is a possibility that the reduced infall may be due to the galaxy wide outflows implemented in the simulations.

The main challenge in comparing these simulated results with the observed Keck + VLRS correlation functions comes from the presence of velocity errors for the observed LBGs which dominate at $\lesssim 1h^{-1}$Mpc scales. When these are taken into account both real- and z-space LBG correlation functions prefer the high amplitude of clustering shown by higher mass ($M_{*} > 10^{9} M_{\odot}$) galaxies in the simulation. The simulated cross-correlation function shows similar neutral gas densities around galaxies as are seen in the observations. The simulated and observed Lyα z-space autocorrelation functions again agree better with each other than with the $\beta_{Ly\alpha} \approx 1.3$ infall model. Finally, little direct evidence is seen in either simulations or observations for high transmission near galaxies due to feedback in agreement with the results of Rakic et al. However, these authors claim evidence for random peculiar velocities between gas and galaxies at small scales and strong infall at larger scales which are much less evident in our GIMIC simulations or indeed in the observed Keck+VLRS data.

Key words: galaxies: high−redshift , intergalactic medium

1 INTRODUCTION

The effect of feedback via supernovae and AGN driven winds is thought to be a key factor in the process of galaxy formation and evolution. Semi-analytical cosmological models require some injection of feedback to regulate the star formation activity in order to limit both the number of low-mass and high-mass galaxies (White & Rees 1978, White & Frenk 1991). In addition, cosmological smoothed particle hydrodynamics (SPH) simulations from Springel & Hernquist (2003) have shown that galactic outflow from supernova feed-

---

* E-mail: pimpunyawat.tummuangpak@durham.ac.uk back is fundamental to recreating the cosmic star-formation history. It is also evident that simulations lacking some sort of feedback struggle to reproduce realistic disk galaxies (Scannapieco et al. 2012; Schaye et al. 2010; Weil et al. 1998) and that powerful galactic winds are required in order to produce the observed metal enrichment of the IGM (Cen & Ostriker 1999; Theuns et al. 2002; Aguirre et al. 2005; Oppenheimer & Davé 2006).

In terms of observing the effects of feedback at high redshift, Adelberger et al. (2003, A03 hereafter) presented the cross-correlation between $z \sim 3$ galaxies and the IGM (as traced by QSO sightlines) and claimed an observed lack of absorbing gas within $\sim 0.5\ h^{-1}$Mpc. They interpreted this as evidence of strong galactic winds removing HI gas from the vicinity of these star-forming galaxies. The work was based on the Keck HiRES ($R \sim 40,000$) spectra of 8 background QSOs at $z \approx 3$ combined with 431 Lyman Break Galaxies (LBGs) from the survey of Steidel et al. (2003). Following the results of Adelberger et al. (2003), Adelberger et al. (2005, A05 hereafter) updated the result with greater numbers of galaxies, this time centred at $z \sim 2$. Based on this new sample, A05 found increase in Lyα absorption down to scales of r $\sim 0.5\ h^{-1}$ comoving Mpc of LBG positions, with no evidence for HI gas having been removed from the vicinity of these galaxies. Indeed, Crighton et al. (2011) surmised that the cross-correlation at such small scales would likely be affected by uncertainties in the galaxy redshifts in the A03 data. It is therefore still unclear to what extent galactic winds have an effect on the galaxy surroundings.

In addition to the above evidence for gas outflows, gas inflows or infall down to galaxy scales is also expected in simple models of galaxy formation. Gas inflow is expected to be coherent down to the virial radius of a massive galaxy (≈ 50 kpc), below which scale the situation is more complicated due to shocks and the gas pressure becoming more important. Gas flow infall into galaxies along filaments is also expected in secular models of galaxy formation where the gas accretion rate may not be simply dictated by merging rates in a hierarchical model (Dekel et al. 2009). Rakic et al. (2012) presented a study of the galaxy-IGM cross-correlation at $z \approx 2.4$ using 15 fields of the Keck Baryonic Survey. They saw fingers-of-god on sub-100 kpc scales and evidence for infall on larger scales.

In order to constrain simulations of galaxy formation, it is imperative to provide extensive observations of the IGM via hydrogen and metal absorption lines and thus identify and probe the infall and outflow processes. As such, we are undertaking a large galaxy survey centred on distant bright QSOs in the form of the VLT LBG Redshift Survey (VLRS). Bielby et al. (2011) presented the first stage of the galaxy survey, comprising $\approx 1{,}000$ $z \sim 3$ galaxies within $\sim 30'$ of $z > 3$ QSOs. Using this sample, Crighton et al. (2011) performed a cross correlation analysis between the galaxy positions and the Lyα forest of the available QSO spectra in the fields, finding increased absorption within $\sim 5\ h^{-1}$Mpc of galaxy positions. This result was consistent with the results of A03 and A05, but lacked the galaxy numbers to probe the $\sim 0.5\ h^{-1}$Mpc scales at which A03 claimed to see the effects of galaxy winds. Since then, the VLRS has been extended to incorporate ~ 2000 LBGs within 9 separate fields containing bright $z > 3$ QSOs (Bielby et al. 2013), comparable in number to the the only other equivalent surveys at this redshift (e.g. Rakic et al. 2012; Rudie et al. 2012).

In this paper, we update the work of Crighton et al. (2011), adding the galaxy redshifts of Bielby et al. (2011) and also Steidel et al. (2003) in conjunction with the available high-resolution QSO spectra in these survey fields. This work thus combines the higher galaxy sampling rate of the Steidel et al. (2003) survey with the wide fields of the VLRS and provide a galaxy sample that can probe the full range of scales from a few hundreds of kpc to tens of Mpc. This large range of scales is imperative for distinguishing between models of gas inflow and outflow in 2-D galaxy-gas cross-correlation analysis.

Additionally, we use the Galaxies-Intergalactic Medium Interaction Calculation (GIMIC, Crain et al. 2009) simulation to help interpret the above correlation function results. The simulations are used to create synthetic Lyα spectra and galaxies. We study both galaxy clustering and the relationship between gas and galaxies via the (cross-) correlation functions $\xi(s)$ and $\xi(\sigma, \pi)$.

This paper is organised as follows. Observational data from the VLT and Keck surveys are described in section 2. Section 3 describes the GIMIC simulations. The simulated galaxy clustering results and their interpretation are shown in section 4, while the galaxy-IGM cross-clustering and Lyα auto-correlation results are similarly described in section 5. Discussion and conclusions are in section 6 and 7 respectively.

Throughout this work, we use a cosmology with $\Omega_m = 0.30$, $\Omega_\Lambda = 0.70$ and $h_0 = 100\ h$ kms^{-1}Mpc^{-1}. Unless stated otherwise all distances are comoving in units of h^{-1} Mpc, and magnitudes use the AB system.

2 OBSERVATIONS

The data used here are a combination of spectroscopically identified $z \sim 3$ star-forming galaxies and high-resolution spectral observations of the Lyα forest of $z \gtrsim 3$ QSOs.

The galaxy data are a combination of the VLRS data presented by Bielby et al. (2011) and Bielby et al. (2013) and the publicly available Keck LBG data presented by Steidel et al. (2003). We note at this point that the VLRS data offer coverage across large fields of view, effectively tracing the large scale structure across scales of $\sim 30 - 60$ comoving Mpc tangential to the line of sight. In contrast, the Keck sample covers relatively small areas ($\approx 8 - 10$ comoving Mpc), but offer higher sampling rates of the galaxy population. The QSO spectra with which we trace the distribution of HI within the fields have all been obtained from archival VLT UVES and Keck HiRES observations. In this section, we give details of all the data used and the reduction processes used for the QSO spectra.

2.1 LBG Observations

The VLRS currently provides $\sim 2,000$ spectroscopic galaxy redshifts within 9 fields centred on $z \gtrsim 3$ QSOs (Bielby et al. 2011, 2013). The redshifts were obtained using the VLT VIMOS instrument with the LR_Blue grism giving a resolution of $R \sim 180$ and velocity accuracies of $\delta v \sim 350$ kms^{-1}. In total the survey covers an area of ~ 2.6

deg^2 and provides galaxy data in the foreground of the following 9 high redshift QSOs: Q0042-2627 ($z = 3.29$), J0124+0044 ($z = 3.84$), Q0302-0035 ($z = 3.23$), HE0940-1050 ($z = 3.05$), J1201+0116 ($z = 3.23$), PKS2126-158 ($z = 3.28$), Q2231+0015 ($z = 3.02$), Q2348-011 ($z = 3.02$) and Q2359+0653 ($z = 3.23$). The spectroscopic galaxy sample is predominantly limited to $R < 25$ although a number of fainter galaxies ($R < 25.5$) are present in the sample where slit allocation during the VIMOS observations could be optimised by their inclusion.

The LBG redshifts were identified using Lyα emission lines and interstellar medium (ISM) absorption lines where visible. For both the Lyα and ISM features it is necessary to correct the ascertained redshift for intrinsic velocity effects, due to these features originating in outflowing gas (e.g. A03, Steidel et al. 2010). As such the VLRS galaxy redshifts have been corrected according to the prescription given by Steidel et al. (2010).

The Keck survey provides a sample of ~ 940 LBGs observed using the Keck LRIS instrument. The QSOs from six (Q0201+1120, Q0256-0000, Q0302-003, Q0933+2854, Q2233+1341 and Q1422+2309) out of the 17 Keck fields are available to us through the public archive and taking only those galaxies in fields around these 6 Keck QSOs, the numbers of LBGs are reduced to 308. The Keck LBGs are limited to $\mathcal{R} = 25.5$.

2.2 QSO data

We have analysed publicly available archival spectroscopy for 17 QSOs in the redshift range $2.5 < z < 4.0$. The data are all high resolution, high signal-to-noise spectra observed using either the UVES instrument on the VLT or the HiRES instrument on the Keck telescope. Full details of the reduction of UVES and HiRES QSO spectra for 11 of the QSOs used here are provided by Crighton et al. (2011). The remaining 6 spectra were all observed with the Keck HiRES instrument and were reduced following an identical method to that used for the two Keck QSOs of Crighton et al. (2011), using the MAKEE package[1]. Briefly, this encompassed basic flat-fielding and bias subtraction, followed by the use of SPIM2 to splice the echelle orders and combine individual observations. This involved producing template spectra constructed by combining the individual observations, masking bad regions of the CCDs and rescaling. A template was applied to rescale the original observations. We divide out the continuum for each individual observation, then multiply this normalised flux by a continuum fit to the template. After scaling each order of each observation individually, we combined them to get the final spectrum.

In addition to the publicly available QSO spectra, we also include a spectrum from our own observations using the X-Shooter instrument on the VLT (Q2359+0653). This data was reduced using the X-Shooter pipeline package, see Bielby et al. (in prep) for details. The full list of QSOs used in this study is provided in Table 1.

3 GIMIC SIMULATIONS

3.1 Overview

We use gas dynamical simulations to create both Lyα spectra and galaxies to compare with the observational data. Our main aims are to study the real and redshift-space correlation functions to see if we can detect the effects of peculiar velocities to understand more about gas outflow and infall into galaxies, for (a) LBG-LBG pairs (b) the LBG-Lyα forest and (c) Lyα-Lyα pairs. The results will then be used to interpret the observable 1-D and 2-D correlation functions $\xi(s)$ and $\xi(\sigma, \pi)$ in terms of both simulation and observational results.

For this purpose we use the GIMIC simulation, which is a cosmological hydrodynamical re-simulation of selected volumes of the Millennium simulation (Springel 2005). GIMIC is designed to overcome the issues in simulating large cosmological volumes ($L \gtrsim 100h^{-1}$ Mpc) at high resolution ($m_{gas} \lesssim 10^7 h^{-1}$ M$_\odot$) to $z = 0$ by taking a number of smaller regions with 'zoomed' initial conditions (Frenk et al. 1996; Power et al. 2003; Navarro et al. 2004). These individual regions each have approximate radii of $18h^{-1}$Mpc outside of which the remainder of the Millennium simulation volume is modelled with collisionless particles at much lower resolution.

In the work presented here we use only the '0σ' GIMIC region, which is identified as having a mean density at $z = 1.5$ equal to the mean density of the simulation as a whole at that epoch. In addition, we use only one snapshot of this region, chosen to be at a redshift of $z = 3.1$ in order to provide a suitable comparison to our $z \sim 3$ observed population of star-forming galaxies. GIMIC was run using the TreePM SPH code GADGET3, which is an update of the GADGET2 code (Springel 2005). The cosmological parameters adopted were: $\Omega_m = 0.25$, $\Omega_\lambda = 0.75$, $\Omega_b = 0.045$, $h_0 = 100\ h\ \text{kms}^{-1}\text{Mpc}^{-1}$, $h = 0.73$, $\sigma_8 = 0.9$ and $n_s = 1$ (where n_s is the spectral index of the primordial power spectrum). We note also that the GIMIC simulation does not incorporate the effects of AGN feedback but, importantly, does implement a prescription for supernovae driven feedback.

Although the GIMIC volume is small, it still can be useful for studying $z - space$ distortions. This is because in the simulations we have knowledge about the real-space correlation functions and so we do not need an ensemble average over a large volume to guarantee spherical symmetry.

3.2 Simulated galaxy population

The galaxy population is identified in the simulation based on first identifying the dark matter halos using a Friends of Friends (FoF, Davis et al. 1985) algorithm. A group finding algorithm then locates the nearest dark matter halo for each baryonic (gas or star) particle and identifies the particle with this halo. The SUBFIND algorithm (Springel et al. 2001; Dolag et al. 2009) is then used to identify self-bound sub-structures within the halos, to which star particles are associated and defined as galaxies.

Given a limiting radius for our galaxy sample within the GIMIC volume of 16 h^{-1} Mpc radius simulation volume and a stellar mass limit of $M_\star \geqslant 10^8$ M$_\odot$ we obtain a total of 4,070 galaxies from the snapshot at $z = 3.06$ in

---

[1] http://www2.keck.hawaii.edu/inst/hires/makeewww/

QSO	R.A.	Dec.	z	Mag	Instrument
	J2000				
Q2359+0653	00:01:40.6	+07:09:54	3.23	$V = 18.5$	X-Shooter
Q0042-267	00:44:33.9	-26:11:19	3.289	$B = 18.5$	HIRES
J0124+0044	01:24:03.8	+00:44:32	3.83	$g = 19.2$	UVES
Q212904.90-160249.0	21:29:04.90	-16:02:49.0	2.90	19.2	HIRES
$[WHO91]$0043-265	00:45:30.470	-26:17:09.20	3.44	18.34	HIRES
Q0201+1120	02:03:46.7	+11:34:45	3.610	20.1	HIRES
Q0256-0000	02:59:05.6	+00:11:22	3.364	18.2	HIRES
LBQS 0301-0035	03:03:41.0	-00:23:22	3.230	17.6	HIRES
Q0302-0019	03:04:49.9	-00:08:13	3.281	17.8	HIRES
QSO B0933+289	09:33:37.2	+28:45:32	3.428	17.8	HIRES
HE0940-1050	09:42:53.5	-11:04:25	3.06	$B = 17.2$	UVES
J1201+0116	12:01:44.4	+01:16:11	3.233	$g = 17.7$	HIRES
PKS2126-158	21:29:12.2	-15:38:40	3.268	$V = 17.3$	UVES
Q2231-0015	22:34:08.9	+00:00:01	3.02	$r = 17.3$	UVES
Q2233+136	22:36:27.2	+13:57:13	3.209	18.7	HIRES
Q2348-011	23:50:57.9	-00:52:10	3.023	$r = 18.7$	UVES
Q1422+2359	14:24:38.1	+22:56:01	3.620	16.5	HIRES

Table 1. List of QSOs used in this study.

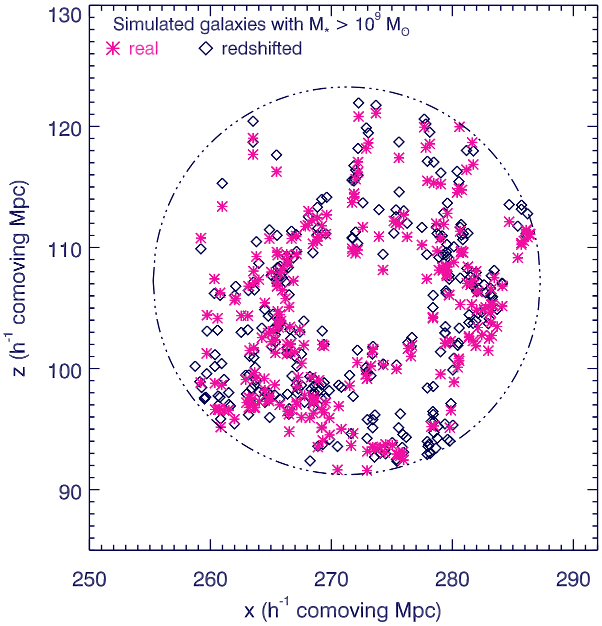

Figure 1. The distribution of $M_\star \geqslant 10^9$ M$_\odot$simulated galaxies in real-space (pink asterisks) and redshift-space(diamonds).

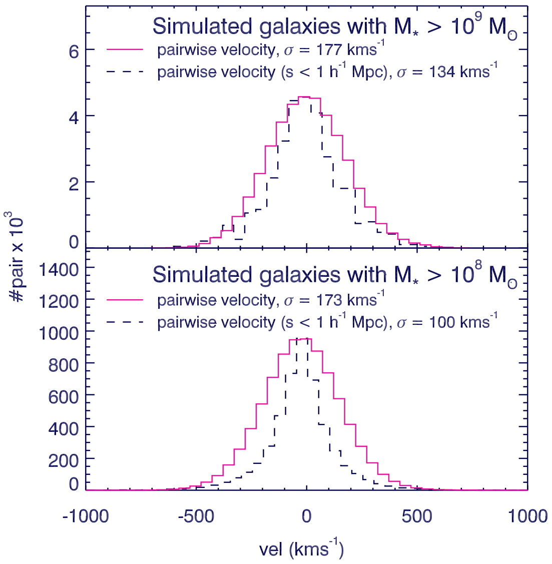

Figure 2. The histograms of pairwise velocities (Δv_z) (pink histograms) from the full sample and from the $s < 1$ h^{-1} Mpc sample of galaxy pairs (blue dashed histograms) for the high and low mass galaxy samples.

the 0σ density region. A number of studies have investigated the mass distribution of LBGs at $z \approx 2-3$, suggesting median stellar masses for galaxies selected in this way of $M_\star \sim 1.4{\times}10^{10}$ M$_\odot$, with a scatter of $\sim \log_{10}(M/\mathrm{M}_\odot) \sim 0.5$ (Shapley et al. 2005). However, at such masses, the galaxy population in GIMIC is too small for the analysis we wish to perform and therefore a compromise is required. We therefore choose a mass cut of $M_\star \geqslant 10^9$ M$_\odot$ to provide our closest feasible estimate of the LBG population. The effect of choosing a relatively low mass cut is somewhat mitigated by the relatively high value of σ_8 used in the GIMIC simulations, which acts to increase the simulated clustering. Thus, although the mass cut is a little low, the clustering of the simulated sample should be comparable to the observed LBG population, given the large σ_8 in GIMIC. Doing so gives a sample of $M_\star \geqslant 10^9$ M$_\odot$ galaxies with $r \leqslant 16h^{-1}$ Mpc of the simulation volume, giving a space density of $\rho_g \sim 5 \times 10^{-3}$ cMpc^{-3} and 287 galaxies. This is marginally higher than, but still comparable to, the observed number densities of LBG galaxies (Adelberger et al. 2005).

The distribution of $M_\star \geqslant 10^9$ M$_\odot$ galaxies in real- (diamonds) and redshift-space (asterisks) is shown in Fig. 1. Throughout this paper, we will assume that the x and y coordinates give positions tangential to the line of sight, whilst z coordinates give the line of sight positions, either in real

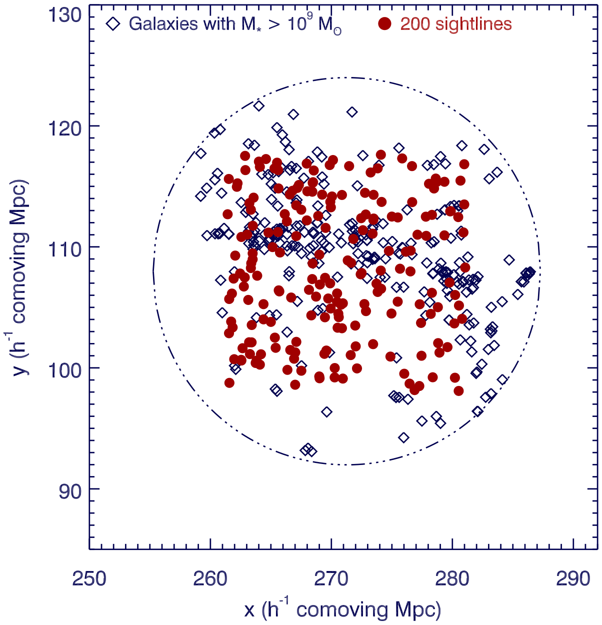

Figure 3. The projected position of $M_\star \geqslant 10^9$ M$_\odot$ galaxies (diamonds) and 200 Lyα sightlines (circles) on the XY plane.

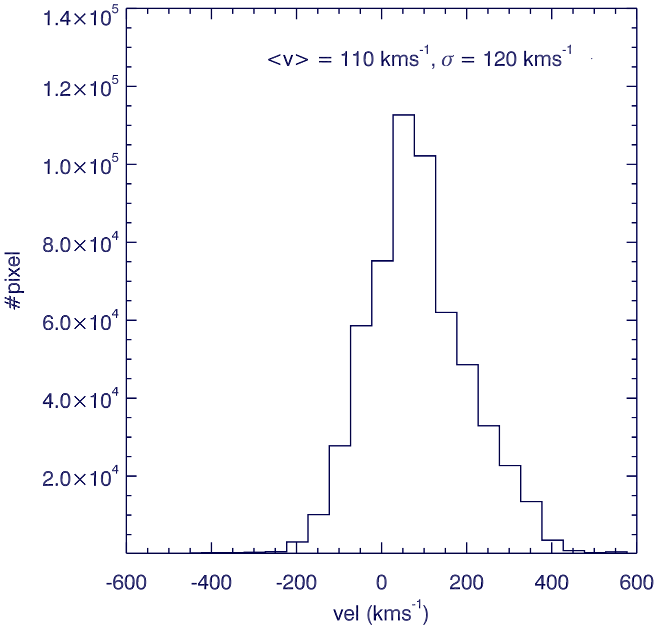

Figure 5. The distribution of LOS mass weighted peculiar velocities measured within each pixel in each of the GIMIC simulated spectra. This illustrates the underlying dynamics present in the spectra. The LOS peculiar velocity distribution shows a mean peculiar velocity of $\langle v_z \rangle = 110$ kms^{-1} with a standard deviation of 120 kms^{-1}.

or redshift-space. Fig. 1 illustrates the measured positional shifts in the z-axis given by the peculiar velocities of the galaxies within the simulation. It is evident from this plot that there is a consistent 'bulk' motion directed in the positive z-direction. Measuring the distribution of the galaxy velocities, we find an average velocity $\langle v_z \rangle = 93$ kms^{-1} with a standard deviation of 128 kms^{-1} for the $M_\star \geqslant 10^9$ M$_\odot$ galaxy sample and $\langle v_z \rangle = +94$ kms^{-1} with a standard deviation of 125 kms^{-1} for the $M_\star \geqslant 10^8$ M$_\odot$ galaxy sample.

We show the pairwise velocity (Δv_z) distributions (pink histograms) of galaxies in Fig. 2. For the $M_\star \geqslant 10^9$ M$_\odot$ and $M_\star \geqslant 10^8$ M$_\odot$ galaxy samples we find a standard deviation of $\sigma_v = 177$ kms^{-1} and $\sigma_v = 173$ kms^{-1} respectively. The blue dashed histograms show the distribution for only those pairs within $r = 1$ h^{-1}Mpc of each other, thus isolating the intra-halo velocity dispersion and excluding the effect of the halo-halo velocity dispersion. This is important when considering the effect of the velocity dispersion on the galaxy-galaxy clustering measurement. The standard deviations of the pairwise velocities for pairs within $s \leqslant 1$ h^{-1}Mpc are 134 kms^{-1} and 100 kms^{-1} for $M_\star \geqslant 10^9$ M$_\odot$ and $M_\star \geqslant 10^8$ M$_\odot$ galaxies respectively. None of these standard deviations include redshift uncertainties due to measurement errors that affect the observed galaxy redshifts.

3.3 Simulating Lyα forest spectra

We next generated spectra along the z-direction through the GIMIC volume to compare with the observations. The sightlines were extracted using SPECWIZARD[2]. The transmission is given by, $T = e^{-\tau}$, where τ is the optical depth along the line-of-sight. We use a spectral resolution FWHM of 7.0 kms^{-1} to convolve each spectrum, a signal-to-noise of 50 per pixel, and pixels of width 2.8 kms^{-1} which are typical values of our UVES and HIRES QSO spectra. The sightlines were generated with random X, Y positions, then parallel to the $Z-$axis. We constructed 200 sightlines, with this number providing an approximate optimum between maximising the statistics available and minimising the over-sampling of any region of the volume. Each sightline was constrained to not extend beyond 16 h^{-1} Mpc from the centre of the GIMIC volume in order to avoid any edge effects in terms of the gas extent. The average transmission, $\bar{T}_r$ for real space is 0.69 while the $\bar{T}_z$ for redshift-space is 0.72. An explanation for this difference is that infall of saturated absorption lines towards each other in redshift-space may result in an overall increase in the measured flux. This will cause the average transmissivity over the full spectrum to increase in redshift-space as seen. Some hint of this effect can be seen in Fig. 4 in which we show a number of examples of the flux from each sightline compared in real and redshift-space.

Using SPECWIZARD, we calculate the mass weighted line-of-sight (LOS) peculiar velocities for each pixel in our 200 spectra. The distribution of the peculiar velocities is given in Fig. 5. As with the galaxy population, the gas traced by the simulated spectra shows the bulk motion in the positive z-direction, with a mean peculiar velocity of $\langle v_z \rangle = 110$ kms^{-1} and a standard deviation of 120 kms^{-1}.

---

[2] Developed by J. Schaye, C. Booth and T. Theuns, refer to Theuns et al. (1998) for details

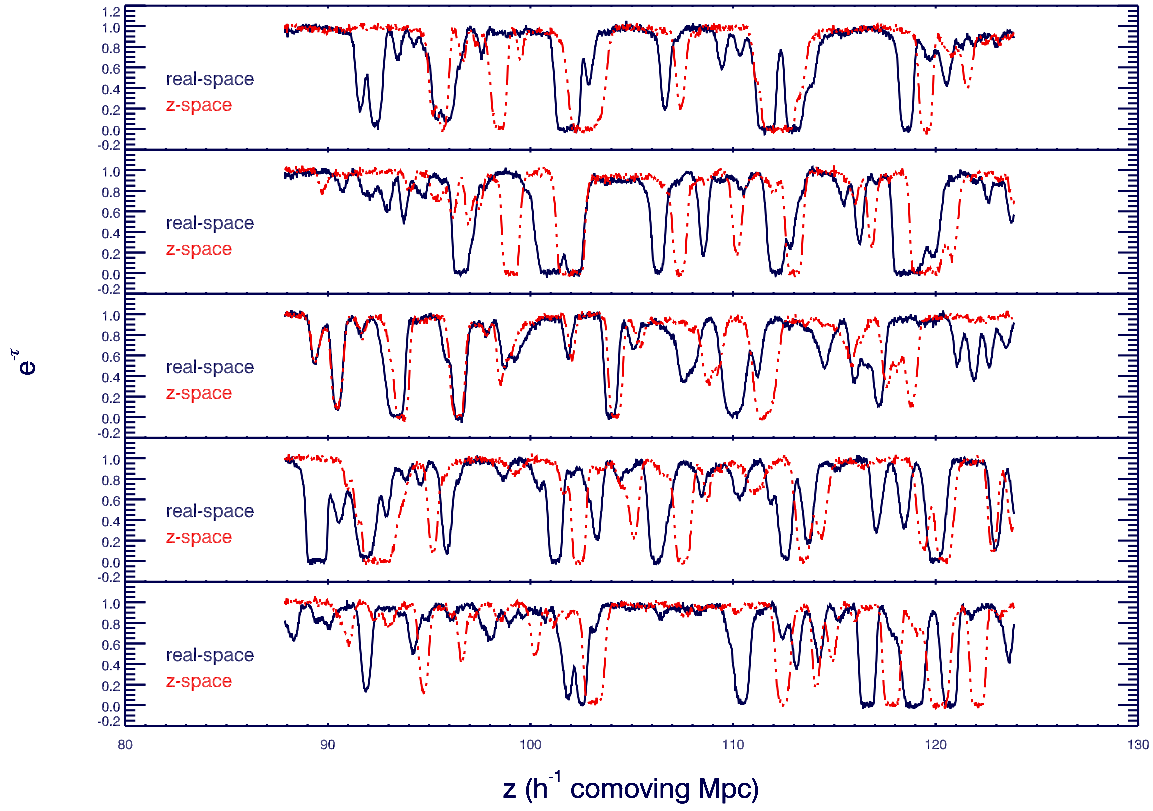

Figure 4. Examples of absorption spectra from simulated QSO sightlines. The blue solid line shows $e^{-\tau}$ in real space the red dashed line shows $e^{-\tau}$ in redshift-space.The scale is measured in h^{-1} comoving Mpc.

4 GALAXY CLUSTERING

4.1 1-D correlation function

4.1.1 Estimator

Bielby et al. (2013) presented a clustering analysis of the LBG data used in this study (combining the VLRS and Keck data). In this section, we compare the observed galaxy clustering presented by Bielby et al. (2013) to results obtained using the galaxy population within the GIMIC simulation. In so doing, we may validate how representative the GIMIC galaxy population is of the observed $z \approx 3$ LBG population in terms of intrinsic clustering properties and the effects of the galaxy velocity field on the galaxy clustering.

We calculate the real and redshift-space functions, $\xi(r)$ and $\xi(s)$, of the GIMIC $z = 3.06$ galaxy samples using the estimator:

$$\xi(r) = \frac{N_R}{N_G}\frac{\langle DD(r)\rangle}{\langle DR(r)\rangle} - 1 \qquad (1)$$

where $\langle DD(s)\rangle$ is the average number of galaxy-galaxy pairs, $\langle DR(s)\rangle$ is the number of pairs of galaxy-randoms at the separation, r, where we use r to represent the separation in real space and s the separation in redshift-space. The factor $\frac{N_R}{N_G}$ is the ratio of the number of random to data points.

We estimate errors on the auto-correlation results using jack-knife estimates based on splitting the simulation into equal volume octants and excluding each octant in turn to create 8 jack-knife realisations of the data. The correlation functions are then fit using a power-law of the form of:

$$\xi(r) = \left(\frac{r}{r_0}\right)^{-\gamma} \qquad (2)$$

where γ is the slope of real-space clustering, $\xi(r)$, and r_0 is the real-space clustering length.

4.1.2 Simulated real-space galaxy correlations

Fig. 6 shows the results for the simulated galaxy-galaxy correlation function with (a) $M_\star \geqslant 10^9$ M$_\odot$ and (b) $M_\star \geqslant 10^8$ M$_\odot$ simulated galaxies. The blue diamonds show results from galaxies in redshift-space while the pink asterisks show results from galaxies in real space. The integral constraint, $\mathcal{I}$, is included in the data in order to compensate for the effect of the limited field sizes (as described in Bielby et al. 2013). The estimated integral constraints are $\mathcal{I} = 0.21$ and $\mathcal{I} = 0.11$ for $M_\star \geqslant 10^9$ M$_\odot$ galaxies and the full sample respectively. The pink lines represent power-law fits to the real-space correlation function based on Eqn. 2 with $\gamma = 1.56 \pm 0.26$ and $r_0 = 4.16 \pm 1.16$ h^{-1}Mpc in the $M_\star \geqslant 10^9$ M$_\odot$ galaxies' plot while $\gamma = 1.52 \pm 0.10$, $r_0 = 2.41 \pm 0.24$ h^{-1}Mpc in $M_\star \geqslant 10^8$ M$_\odot$ galaxies' plot. These power-law results give good fits to the real-space clustering results and we note that there is little sign of a double

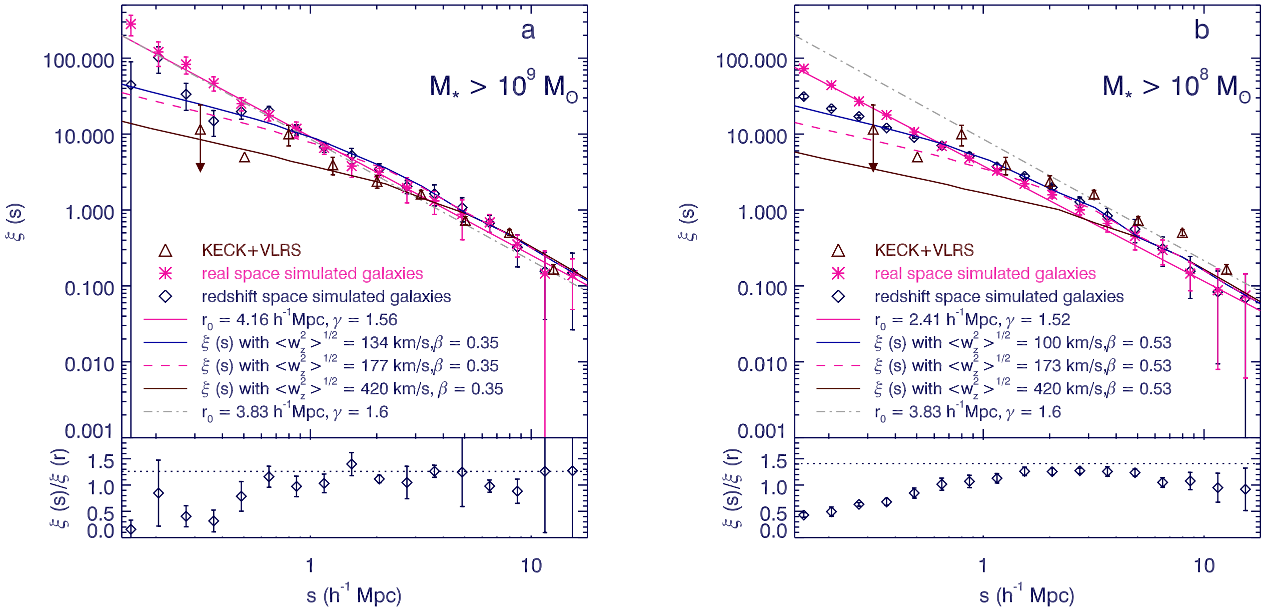

Figure 6. (a) Galaxy correlation functions for 287 simulated $M_\star \geqslant 10^8$ M$_\odot$ galaxies compared to the observed LBGs. Real space - pink asterisks, redshift-space - blue diamonds, LBG data - brown triangles. Also shown are fits to simulated real space (pink line) with $\gamma = 1.56$ and $r_0 = 4.16$ h^{-1}Mpc. The real-space fit to the Keck+VLRS data is shown by the grey dot-dashed line. The pink dashed line is the predicted $\xi(s)$ assuming the real-space fit with the full pairwise velocity dispersion of $\langle w_z^2 \rangle^{1/2} = 177$ kms^{-1}. The blue solid line is the same except with the $s < 1$ h^{-1} Mpc pairwise dispersion of $\langle w_z^2 \rangle^{1/2} = 134$ kms^{-1}. The brown line is the same model now with $\langle w_z^2 \rangle^{1/2} = 420$ kms^{-1}, with velocity errors added to allow comparison with the Keck+VLRS LBG $\xi(s)$. (b) The same for 4,070 simulated $M_\star \geqslant 10^8$ M$_\odot$ galaxies with real space fit $\gamma = 1.52$, $r_0 = 2.41$ h^{-1}Mpc. The $\xi(s)$ predictions now assume the appropriate pairwise velocity dispersion of $\langle w_z^2 \rangle^{1/2} = 173$ kms^{-1} (pink dashed line) and $\langle w_z^2 \rangle^{1/2} = 100$ kms^{-1} (blue solid line). Bottom panels present $\xi(s)/\xi(r)$ with jack-knife error bars. The dotted line represents the predicted Kaiser boost (Kaiser et al. 1987) with (a) $\beta = 0.35$ giving $\xi(s)/\xi(r) = 1.26$ for $M_\star \geqslant 10^9$ M$_\odot$ galaxies and the Kaiser boost with (b) $\beta = 0.53$ giving $\xi(s)/\xi(r) = 1.41$ for $M_\star \geqslant 10^8$ M$_\odot$ galaxies.

power-law or two-halo break in the clustering for either of the samples. The contribution of the single halo term in galaxy clustering is generally seen to be more significant with higher galaxy stellar mass however and so the lack of any break may be due to the mass constraints used here. This result should clearly be checked in bigger simulations.

4.1.3 Simulated $\xi(s)/\xi(r)$ and infall

In the lower panels we show the ratio between the real and redshift-space clustering results in order to highlight the signatures of redshift-space distortions in the redshift-space correlation function. Here the errors are again constructed from the jack-knife realisations. At scales above $s \sim 1.5 - 2$ h^{-1}Mpc, we see the effects of dynamical infall, which acts to boost the clustering signal in the redshift-space measurement. From linear theory (Kaiser 1987; Hamilton 1992) we expect to see the 'Kaiser boost', which is given given by:

$$\xi(s) = (1 + \frac{2}{3}\beta + \frac{1}{5}\beta^2)\xi(r) \qquad (3)$$

where β is the dynamical infall parameter. For galaxies, $\beta = \Omega^{0.6}/b$ where $b = \sqrt{\xi_{gg}/\xi_{mm}}$ is the linear bias parameter. At $z \approx 3$, we proceed via the volume averaged clustering amplitude, $\bar{\xi}(8)$, (see eqns 17, 18 of Bielby et al. 2013). For the $M_\star \geqslant 10^9$ M$_\odot$ simulated galaxy case, the above power-law parameters fitted to $\xi(r)$ give $\bar{\xi}_g(8) = 0.75 \pm 0.05$ which with $\bar{\xi}_{DM}(8) = 0.088$ gives bias $b = 2.80 \pm 0.18$. Taking $\Omega_m(z = 3.0) = 0.98$ gives $\beta = 0.35 \pm 0.02$. So the expected value of the Kaiser boost is 1.26 ± 0.12 compared to the observed amplitude ratio at $1 < s < 8$ h^{-1}Mpc of 1.17 ± 0.06.

Assuming the power-law fitted to $\xi(r)$ for the set of $M_\star \geqslant 10^8$ M$_\odot$ galaxies, we find $\bar{\xi}_g(8) = 0.33 \pm 0.02$, giving $b = 1.85 \pm 0.12$ and $\beta = 0.53 \pm 0.03$. The predicted Kaiser boost is therefore $\xi(s)/\xi(r) = 1.41 \pm 0.14$. At separations of $1 < s < 8$ h^{-1}Mpc, we find a mean amplitude ratio of 1.26 ± 0.03, consistent at the $\sim 1\sigma$ level with a Kaiser boost, although marginally lower than predicted by linear theory. We conclude that for the simulation, the ratio, $\xi(s)/\xi(r)$, is in reasonable agreement with linear theory infall predictions for both high and low mass galaxies.

4.1.4 Simulated galaxy correlations and velocity dispersion

At smaller separations ($r < 1$ h^{-1} Mpc) for both high- and low-mass simulated galaxies, the galaxy-galaxy $\xi(s)$ in redshift space has lower clustering than $\xi(r)$. This turn-over of the real space correlation function is the result of z-space smoothing due to the peculiar velocity dispersion, $\langle w_z^2 \rangle^{1/2}$.

We model the effects of the velocity dispersion on the clustering results using a gaussian distribution to the velocity dispersion, following previous work (e.g. Hawkins et al. 2003; da Ângela et al. 2005). Using the pairwise velocity dispersions derived from Fig. 2 for the two samples (i.e. $\langle w_z^2 \rangle^{1/2} = 177$ kms^{-1} and $\langle w_z^2 \rangle^{1/2} = 173$ kms^{-1} for the $M_\star \geqslant 10^9$ M$_\odot$ and $M_\star \geqslant 10^8$ M$_\odot$ samples respectively - pink dashed lines in both panels), we find that the reduction of the real-space clustering at small scales is overpredicted compared to the measurements of $\xi(s)$. As illustrated in Fig. 2 however, we note that the measured pairwise velocity dispersion is separation dependent. The observed discrepancy is therefore likely the result of the effect of small scale peculiar motions on the clustering function being dominated by galaxies within ~ 1 h^{-1} Mpc of each other, whereas the initial pairwise velocity histogram presented in Fig. 2 includes pairwise velocities between galaxies across all separation scales within the simulation. If we thus limit the histogram of pairwise velocities to only those pairs within 1 h^{-1} Mpc of each other (dashed histograms in Fig. 2), we retrieve pairwise velocity dispersions of $\langle w_z^2 \rangle^{1/2} = 134$ kms^{-1} and $\langle w_z^2 \rangle^{1/2} = 100$ kms^{-1} for the $M_\star \geqslant 10^9$ M$_\odot$ and $M_\star \geqslant 10^8$ M$_\odot$ samples respectively. Using these values in the redshift-space distortion model, we find improved agreement between the model (solid blue line in Fig. 6) and the galaxy auto-correlation function measured from the GIMIC simulations. Ultimately, the appropriate velocity dispersion for modelling the redshift-space distortion effects on the galaxy clustering, is the velocity dispersion present within groups, whilst the peculiar velocity measured from the simple histogram case included the imprint of the velocity dispersion of galaxy groups as well as the dispersion within groups. Taking the histogram of only pairs of galaxies within ~ 1 h^{-1} Mpc of each other effectively measures the intra-group peculiar velocities. We conclude that $\xi(s)$ is better explained on sub-Mpc scales with the intra-group velocity dispersion appropriate for these scales.

4.2 Simulated and observed correlation functions compared

Bielby et al. (2013) report the best fit scale-length and slope for the observed Keck + VLRS LBG-LBG semi-projected $w_p(\sigma)$ for the data is $r_0 = 3.83 \pm 0.24$ h^{-1} Mpc with a slope of $\gamma = 1.60 \pm 0.09$. Within the reported errors, the clustering of our $M_\star \geqslant 10^9$ M$_\odot$ sample reproduces the observed survey clustering very well in terms of both clustering length and slope. As would be expected, the $M_\star \geqslant 10^8$ M$_\odot$ sample gives a somewhat lower clustering length than the observational data, but does at least have a consistent slope within the quoted errors.

We now apply the measured $\langle w_z^2 \rangle^{1/2}$ from the observations of Bielby et al. (2013) to our correlation functions measure from GIMIC. Bielby et al. (2013) measured $\langle w_z^2 \rangle^{1/2} = 420$ kms^{-1}, which includes both the intrinsic velocity dispersion and the velocity errors on measuring the galaxy redshifts. The measured $\xi(s)$ from Bielby et al. (2013) is shown in Fig. 6 (brown triangles) and a model based on the GIMIC $\xi(r)$ combined with the observational $\langle w_z^2 \rangle^{1/2} = 420$ kms^{-1} is given by the brown solid line. By introducing the observationally measured pairwise velocity errors to the GIMIC $M_\star \geqslant 10^9$ M$_\odot$ result, we find that the GIMIC clustering measurement reproduces the measured LBG clustering well.

4.3 2-D correlation function

We now turn to the 2-D galaxy auto-correlation functions in order to further investigate the impact of galaxy velocities on clustering measurements within the simulation. In the 2-D correlation function, $\xi(\sigma, \pi)$, we parameterise the line of sight separation between two galaxies by π and the transverse separation by σ. We calculate $\xi(\sigma, \pi)$ using the same methods as used for the 1-D correlation functions and with the same samples.

Fig. 7 show the 2-D galaxy-galaxy correlation function, $\xi(\sigma, \pi)$, for $M_\star \geqslant 10^9$ M$_\odot$ and $M_\star \geqslant 10^8$ M$_\odot$ simulated galaxies and the results of fitting each of these for $\langle w_z^2 \rangle^{1/2}$ and β, using the 1-D measured clustering lengths and slopes. Panels (a) and (b) show the measured correlation function for the $M_\star \geqslant 10^9$ M$_\odot$ galaxy sample in real- and redshift-space respectively while panels (c) and (d) show the correlation function for the $M_\star \geqslant 10^8$ M$_\odot$ galaxy sample. Note that the previously determined integral constraints are applied in these plots.

Panels (e) and (f) show chi-square contours based on fitting the $M_\star \geqslant 10^9$ M$_\odot$ galaxy $\xi(\sigma, \pi)$ for velocity dispersion and β, based on the real-space $\xi(r)$ (i.e. $r_0 = 4.16$ h^{-1}Mpc and $\gamma = 1.56$). The best fit for real space was $\beta = 0.02$ and velocity dispersion $= 200$ kms^{-1} with reduced $\chi^2 = 0.7$. As expected, there is little significant effect of peculiar velocities seen in real space. In redshift-space, we found $\beta = 0.02$ and the velocity dispersion $= 100$ kms^{-1} with reduced $\chi^2 = 0.7$. Here we are expecting $\beta \approx 0.35$ given the bias, $b = 2.80$, and this is significantly different from what we find in the simulation. But the value of $\beta = 0.02$ from fitting $\xi(\sigma, \pi)$ is also lower than the $\beta = 0.24 \pm 0.1$ implied by the ratio of $\xi(s)/\xi(r)$ above which is in much better agreement with the expected $\beta = 0.35$. For $M_\star \geqslant 10^8$ M$_\odot$ galaxies, we fit the model with $\gamma = 1.52$ and $r_0 = 2.41$ h^{-1}Mpc. The best fit for real space gives $\beta = 0.15$, velocity dispersion $= 80$ kms^{-1}, and reduced $\chi^2 = 0.4$, with β consistent with zero as expected and $\beta = 0.45$, velocity dispersion $= 120$ kms^{-1} with reduced $\chi^2 = 1.1$ for redshift-space as shown in panels (g) and (h). In this case, we are expecting $\beta \approx 0.53$ given the bias, $b = 1.85$. Thus here the fit to $\xi(\sigma, \pi)$ is in much better agreement with linear infall theory. Indeed, a model that assumes the above $\xi(r)$ parameters with $\beta = 0.53$, $\langle w_z^2 \rangle^{1/2} = 100$ kms^{-1} is only rejected by the data at the 1σ level. We conclude that apart from the $\xi(\sigma, \pi)$ result for the $M_\star \geqslant 10^9$ M$_\odot$galaxies, the 1-D and 2-D correlation results for both high and low mass simulated galaxies are generally in reasonably good agreement with linear infall theory.

Bielby et al. (2013) presented the results for $\xi(\sigma, \pi)$ for the VLRS+Keck LBGs. Again the velocity errors dominated the fits which gave $\beta(z = 3) = 0.38 \pm 0.19$ and $w_z = 420^{+140}_{-160}$ kms^{-1} when $r_0 = 3.83 \pm 0.24$ h^{-1} Mpc and $\gamma = 1.60 \pm 0.09$ was assumed for $\xi(r)$. The value of β is in a range consistent with that measured above for the simulated galaxies.

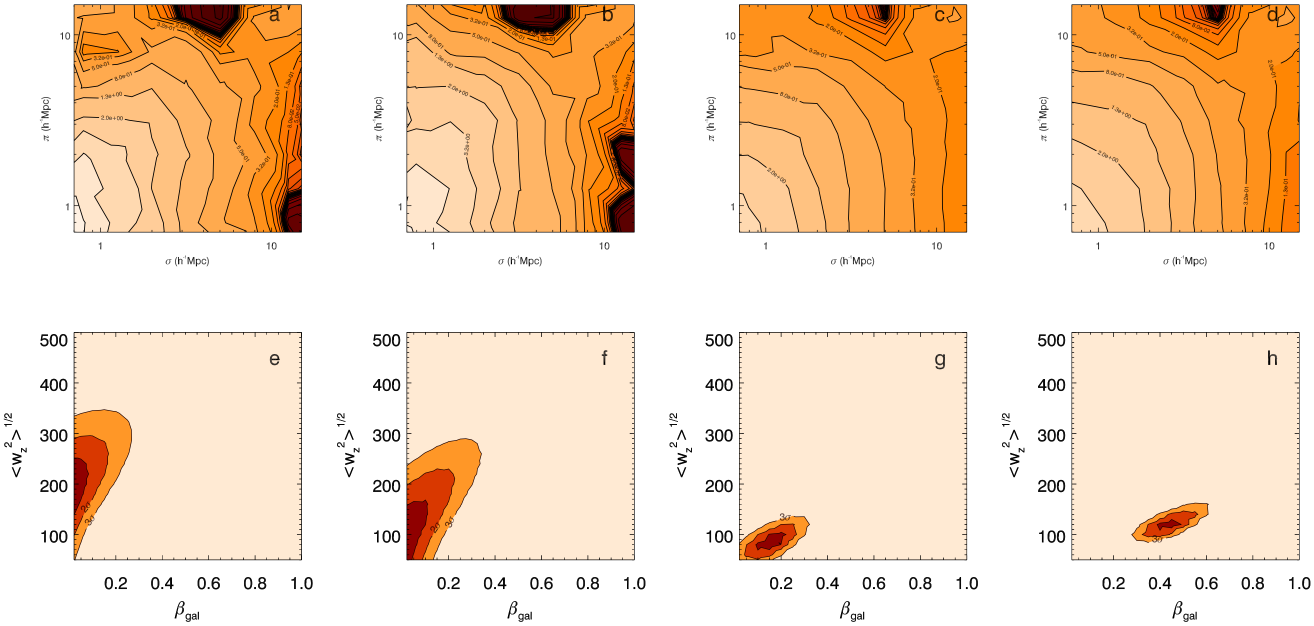

Figure 7. The auto-correlation function $\xi(\sigma, \pi)$ results from simulated galaxies. (a)-(b) are the results from $M_\star \geqslant 10^9$ $\mathrm{M}_\odot$ galaxies in real- and redshift-space respectively. (c)-(d) are the results from $M_\star \geqslant 10^8$ $\mathrm{M}_\odot$ galaxies. (e)-(f) are the pairwise velocity dispersion ($\langle w_z^2 \rangle^{1/2}$)-infall parameter ($\beta$) $\Delta\chi^2$ contours for $\xi(\sigma, \pi)$ with $M_\star \geqslant 10^9$ $\mathrm{M}_\odot$ galaxies, fitting to $\xi(\sigma, \pi)$ with $s < 12$ h^{-1}Mpc. The best fit for (e) real-real gives $\beta = 0.02$, $\langle w_z^2 \rangle^{1/2} = 200$ kms^{-1}, assuming $r_0 = 4.16$ h^{-1}Mpc and $\gamma = 1.56$. The best fit for (f) $z - z$ gives $\beta = 0.02$, $\langle w_z^2 \rangle^{1/2} = 100$ kms^{-1}. (g)-(h) show similar contour plots with (e)-(f) but with $M_\star \geqslant 10^8$ $\mathrm{M}_\odot$ galaxies. The best fit for (g) real-real gives $\beta = 0.15$, $\langle w_z^2 \rangle^{1/2} = 80$ kms^{-1}, assuming $r_0 = 2.41$ h^{-1}Mpc and $\gamma = 1.52$ while the best fit for (h) $z - z$ gives $\beta = 0.45$, $\langle w_z^2 \rangle^{1/2} = 120$ kms^{-1}.

5 GALAXIES AND THE IGM

As discussed earlier, the relationship between the galaxy population and the IGM is key to understanding galaxy growth and evolution. Galaxies require large halos of gas in order to grow to the large masses we observe at the present day, whilst the supply and regulation of the flow of gas into galaxies dictates the distribution of galaxy masses we observe.

From observations of galaxy winds with speeds of $\gtrsim 300$ kms^{-1} for the LBG population (e.g. via the offsets nebulae and inter-stellar medium spectral features), it is evident that outflowing material exists in these star-forming galaxies (e.g. Pettini et al. 2001; Shapley et al. 2003; Bielby et al. 2011). A number of authors have thus attempted to distinguish the effects of such outflows on the distribution of gas around the $z \sim 2-3$ star-forming galaxy population via the Lyα forest observed in the spectra of background sightlines (e.g. A03, A05, Crighton et al. 2011; Rudie et al. 2012; Rakic et al. 2012).

In this section, we therefore perform an analysis of the cross correlation between galaxies and the Lyα forest within the GIMIC simulation. We apply the same dynamical models as in the previous sections to the cross-correlation analysis. However, in the case of the galaxy-gas cross-correlation the relation between redshift and real-space correlations will become $\xi(s)/\xi(r) = (1 + \frac{1}{3}(\beta_{gal} + \beta_{Ly_\alpha}) + \frac{1}{5}\beta_{gal}\beta_{Ly_\alpha})$ (see Mountrichas & Shanks 2007). The linear bias of the gas obtained from $b^2 = \xi_{Ly\alpha-Ly\alpha}/\xi_{mm}$ is $b \approx 0.3$ but this is not the bias required to assess the effect of gas infall via β_{Ly_α}. This is because of the non-linear relation $F = \exp(-\tau)$ between Lyα transmission and optical depth, τ, where most of the physics in the Lyα forest is contained in τ. According to McDonald et al (2000, 2003) the infall parameter $\beta_{Ly_\alpha} = \Omega_m^{0.6} \times b_\eta / b_\delta$ and b_η and b_δ have to be defined from simulations. McDonald (2003) found results for $\beta_{Ly_\alpha} = 1 - 1.6$ depending on the resolution of the simulations. We therefore took $\beta_{Ly_\alpha} = 1.3$ as our estimate of the gas dynamical infall parameter. McDonald (2003) did not use the z-space distortion techniques used here so this and the fact that we are using higher resolution SPH simulations makes it interesting to check whether linear theory with their $\beta_{Ly\alpha}$ fits our simulated data. McDonald et al. (2000) argue that the form of the flux correlation function is proportional to the mass correlation function in the linear regime. Following McDonald (2003), on this basis we shall assume that we can take account of 'finger-of-God' velocity dispersions in the usual way by convolving the transmission correlation function with a Gaussian of the appropriate dispersion.

5.1 Keck+VLRS LBG-Lyα cross-correlation

5.1.1 1D cross correlation, $\langle T(s) \rangle$

To measure the velocity dispersion of HI gas that caused an increase in Lyα absorption at the redshifts, we calculated the Lyα flux along QSO sightlines. We first calculate the transmissivity of the Lyα forest by

$$T = \frac{f}{f_{con}} \tag{4}$$

where f is the observed flux and f_{con} is the continuum in flux level from Lyα forest.

Following A03, for the observational data we normalised the QSO transmissivities for QSOs at $z \sim 3$ by dividing the measured flux transmissivities, T, by

$$\bar{T}(z) = 0.676 - 0.220(z - 3) \tag{5}$$

where z is the redshift of a given pixel. This normalisation is used to correct for the evolution of flux transmissivity with redshift since the transmissivity is higher at low redshift. To avoid the effect of contamination of Lyα absorption lines, we cut out the spectrum below the Lyβ emission. Thus the spectrum between the Lyβ and Lyα is only used in this calculation. We also excluded the wavelength within 20 $\AA$ of the intrinsic Lyα emission to prevent the proximity effects from the QSOs.

We then use the transmissivity of the Lyα forest as calculated above to perform the Lyα-LBG cross correlation function. The Lyα-LBG cross correlation function is calculated from

$$\langle T(s) \rangle = \frac{\langle DT(s) \rangle}{N(s)} \tag{6}$$

where $\langle DT(s) \rangle$ is the number of galaxy-Lyα pairs weighted by the normalised transmissivity, $T/\bar{T}(z)$, for each separation. $N(s)$ is the number of LBGs that contribute to the cross-correlation function at each separation. This is a slightly different approach from A03 who use a correlation function based on the Landy-Szalay estimator.

In Fig. 8, we present the LBG-Lyα transmissivity correlation function from Keck, VLRS, and combined VLRS+A05 sample compared to the results from A03 and A05. The results from Keck, VLRS and combined samples are shown by diamonds, asterisks and filled circles respectively. The triangles and squares show the results of A03 and A05, respectively. At distances greater than 3 h^{-1}Mpc, we found good agreement with both A03 and A05. We note in passing that our own reductions of the Keck sample HIRES data gives a consistent result with the A03 Lyα-LBG sample. In the case of Fig. 8, we continue to use the published A03/A05 results with their larger number of QSOs. The measured $\langle T(s) \rangle$ increases with separation and reaches the mean value of $\bar{T} = 0.77$. At separations below 3 h^{-1} Mpc, the combined sample seems to have the same trend as A05, with no evidence for a turn-up at $s < 1$ h^{-1}Mpc, a feature that was thought to be evidence for feedback. With the larger sample of LBGs close to QSO sightlines compared to Crighton et al. (2011), we have now strengthened the evidence against feedback strongly affecting Lyα absorption on *Mpc* scales around galaxies.

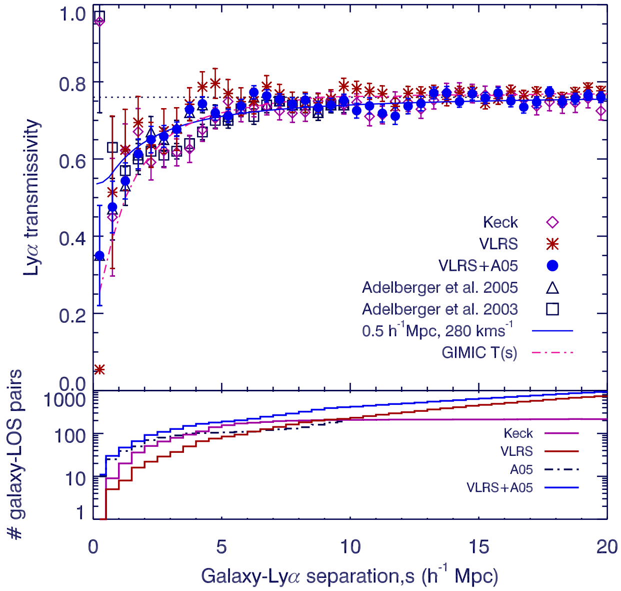

Figure 8. The mean Lyα-Galaxy transmissivity as a function of distance from an average $z \approx 3$ galaxy. Blue filled circles show VLRS+A05 result. Brown asterisks and pink diamonds show results from VLRS and Keck respectively. A03 and A05 are also represented by squares and triangles. The pink dot-dashed line shows the GIMIC $z - z$ result. Also shown is the fit to the $M_{\star} \geqslant 10^8$ M$_{\odot}$ GIMIC Lyα-Galaxy $\langle T(s) \rangle$ from Crighton et al. (2011), with $s_0 = 0.3$ h^{-1}Mpc and $\gamma = 1.0$ (dot-dashed red line). The solid blue line shows this same model convolved with velocity errors of $\langle w_z^2 \rangle^{1/2} = 280$ kms^{-1}. The bottom panel shows the number of LBGs contributing to each bin in each sample.

5.1.2 2-D cross correlation, $\xi(\sigma, \pi)$

We now use the full VLRS sample and Keck LBG-Lyα datasets to measure the 2-D LBG-Lyα cross-correlation, $\xi(\sigma, \pi)$. By combining these two surveys, we can compare the correlation functions in a wider range of separations than would otherwise be possible (the VLRS giving $2-3\times$ the coverage in the σ scale than the Keck data). The LBG-Lyα $\xi(\sigma, \pi)$ from Keck+VLRS sample is presented in Fig. 9.

There is little sign of any 'finger-of-god' effect at small σ scales ($\sigma < 1$ h^{-1}Mpc), i.e. in the form of the clustering power being extended in the π direction. We also present $\Delta\chi^2$ contours from fitting LBG-Lyα $\xi(\sigma, \pi)$ for velocity dispersion and $\beta_{Ly\alpha}$ assuming $\gamma = 1$, $s_0 = 0.3$ h^{-1}Mpc, and $\beta_{gal} = 0.38$. We assumed γ and s_0 from fitting LBG-Lyα $\xi(s)$ using $\xi(s) = (s/s_0)^{-\gamma}$. As shown in Fig. 8, this model reproduces the observed LBG-Lyα $\xi(s)$ results well. We shall therefore take our starting model for the cross-correlation $\xi(r)$ by scaling the above $\xi(s)$ downwards by the expected Kaiser boost of 1.5. We checked that this factor gave the best reduced χ^2 since we are aiming to fit the shape rather than the amplitude of $\xi(\sigma, \pi)$ here. The best fit to $\xi(\sigma, \pi)$ was $\beta_{Ly\alpha} = 0.02$, velocity dispersion $= 20$ kms^{-1}, and reduced $\chi^2 = 0.65$.

We shall return to these Keck+VLRS results to compare with the results from the GIMIC simulations described below. For the moment, we note that the theoretically expected value of the infall parameter is $\beta_{Ly\alpha} = 1.3$ and the expected velocity dispersion, including the effects of LBG velocity error and intrinsic dispersions for gas and galaxies, is $\langle w_z^2 \rangle^{1/2} = \sqrt{297^2 + 120^2} = 320$ kms^{-1}. The observed

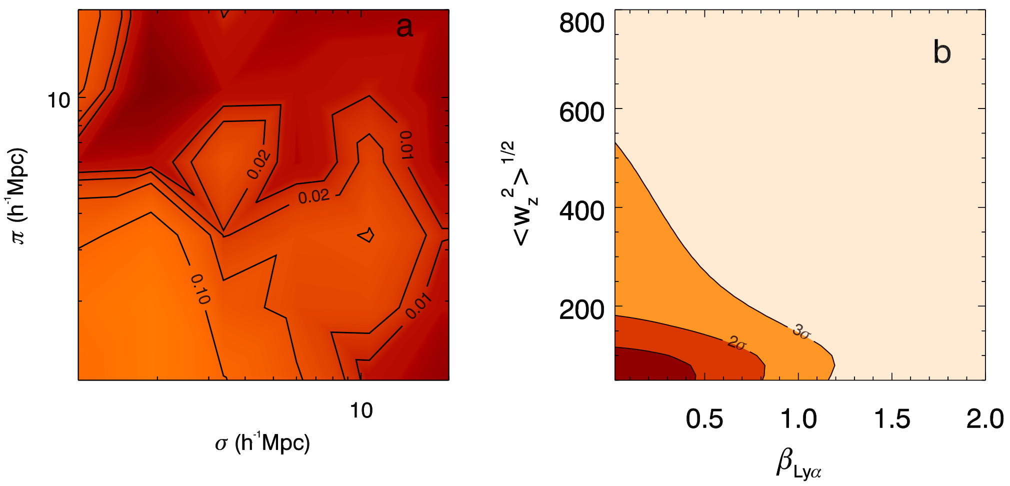

Figure 9. (a) Lyα-LBG $\xi(\sigma,\pi)$ from Keck+VLRS sample. (b) The pairwise velocity dispersion - infall parameter $\Delta\chi^2$ fitting contours for the Keck+VLRS data, fitting to $\xi(\sigma,\pi)$ with $s < 8\ h^{-1}$Mpc. The best fit gives $\beta_{Ly\alpha} = 0.02$, $\langle w_z^2\rangle^{1/2} = 20$ kms^{-1}, assuming $s_0 = 0.3\ h^{-1}$Mpc, $\gamma = 1$ (before correction for Kaiser boost), and $\beta_{gal} = 0.38$.

value of $\beta_{Ly\alpha} = 0.02$ is about 3σ lower than the expected value (see Fig. 9 panel b).

5.2 Lyα-Galaxy $\xi(s)$ from simulations

As with the data, we compute the galaxy-Lyα cross correlation using the methods described above. We note however that the renormalisation to $z = 3$ is here redundant given that the simulated gas and galaxies are all at the same epoch already.

5.2.1 Coherent motion of gas and galaxies

In Fig. 10 (a) we show the Lyα-galaxy $\xi(s)$ for the Lyα in z-space and $M_\star \geqslant 10^9$ M$_\odot$ galaxies in z-space and real space. Fig. 10 (b) shows the same plot but now for the sample of $M_\star \geqslant 10^8$ M$_\odot$ galaxies. Since the high mass sample has poorer statistics here we mainly focus on the $M_\star \geqslant 10^8$ M$_\odot$ sample in Fig. 10 (b) but we believe that the same interpretations apply to both samples. The first thing to note is that the anti-correlation is increased as we go from $r-z$ to $z-z$. This is surprising if we assume that random Gaussian motions dominate galaxy peculiar motions. In this model we expect more smoothing in z-space than in real-space and that is not observed.

Fig. 10 (c and d) shows the Galaxy-Lyα transmissivity correlation function from the Lyα in real- and redshift-space with (c) $M_\star \geqslant 10^9$ M$_\odot$ and (d) $M_\star \geqslant 10^8$ M$_\odot$ galaxies. Focussing on the low mass sample of $M_\star \geqslant 10^8$ M$_\odot$ galaxies, the open diamonds show the results from galaxies in redshift-space and the Lyα in real space while the pink asterisks illustrate the results from galaxies and the Lyα both in real space. At separations $s < 5\ h^{-1}$ Mpc, we see that Galaxy-Lyα transmissivity correlation functions in $z-z$ (light blue squares) and $r-r$ pink asterisks both lie lower than the Lyα-galaxy $r-z$ version (open diamonds). This behaviour is again different from the expected result for random Gaussian motions when the $r-z$ result might be expected to lie between $r-r$ and $z-z$. This and the previous anomaly can be explained by coherent motion when the galaxies and the gas move together and make the correlation from the same space ($z-z$ or $r-r$ space) stronger than the correlation from $r-z$ space combinations. Although the positions of the clouds and the galaxies move, they move coherently so that their relative positions in $r-r$ and $z-z$ remain the same, similar to the effect seen in Fig. 1. This would leave the cross-correlation function the same when redshift or real space was used consistently but undergo smoothing when gas was used in z-space and galaxies in redshift-space or vice versa. Similar but noisier effects are seen in the sample of $M_\star \geqslant 10^9$ M$_\odot$ galaxies in the left-hand panels.

Ignoring the real-z-space combinations, we see that both the real-real and $z-z$ results show the same trends. At a distance $s > 5\ h^{-1}$Mpc, the measured $\langle f/f_{con}\rangle$ increases to reach the mean value. As separations decrease below $5\ h^{-1}$Mpc, the transmissivity decreases and hence the HI density increases as we approach the galaxy.

5.2.2 Dynamical Infall in $\xi(s)$ and $\xi(\sigma,\pi)$

As discussed earlier, we note that the mean transmissivities for the simulated real and redshift-space Lyα forests are somewhat different, with the redshift-space forest having a mean of $\bar{T} = 0.72$ and the real space forest a mean of $\bar{T} = 0.69$. This is surmised to be the result of Lyα absorption lines overlapping increasingly once redshift-space distortions are applied and potentially indicative of infall effects. We shall now discuss dynamical infall of the gas further, by looking for the effect of gas infall on the cross-correlation function.

To better visualise any distortions in the cross-correlation, we calculate the function $\xi = 1 - T/\bar{T}$, using a value of $\bar{T} = 0.69$ in the real-space case and $\bar{T} = 0.72$ in the redshift-space case. The results for $\xi(s)$ are shown in panels (e) and (f) of Fig. 10.

We fit the real-space cross-correlation function $\xi(r)$ by

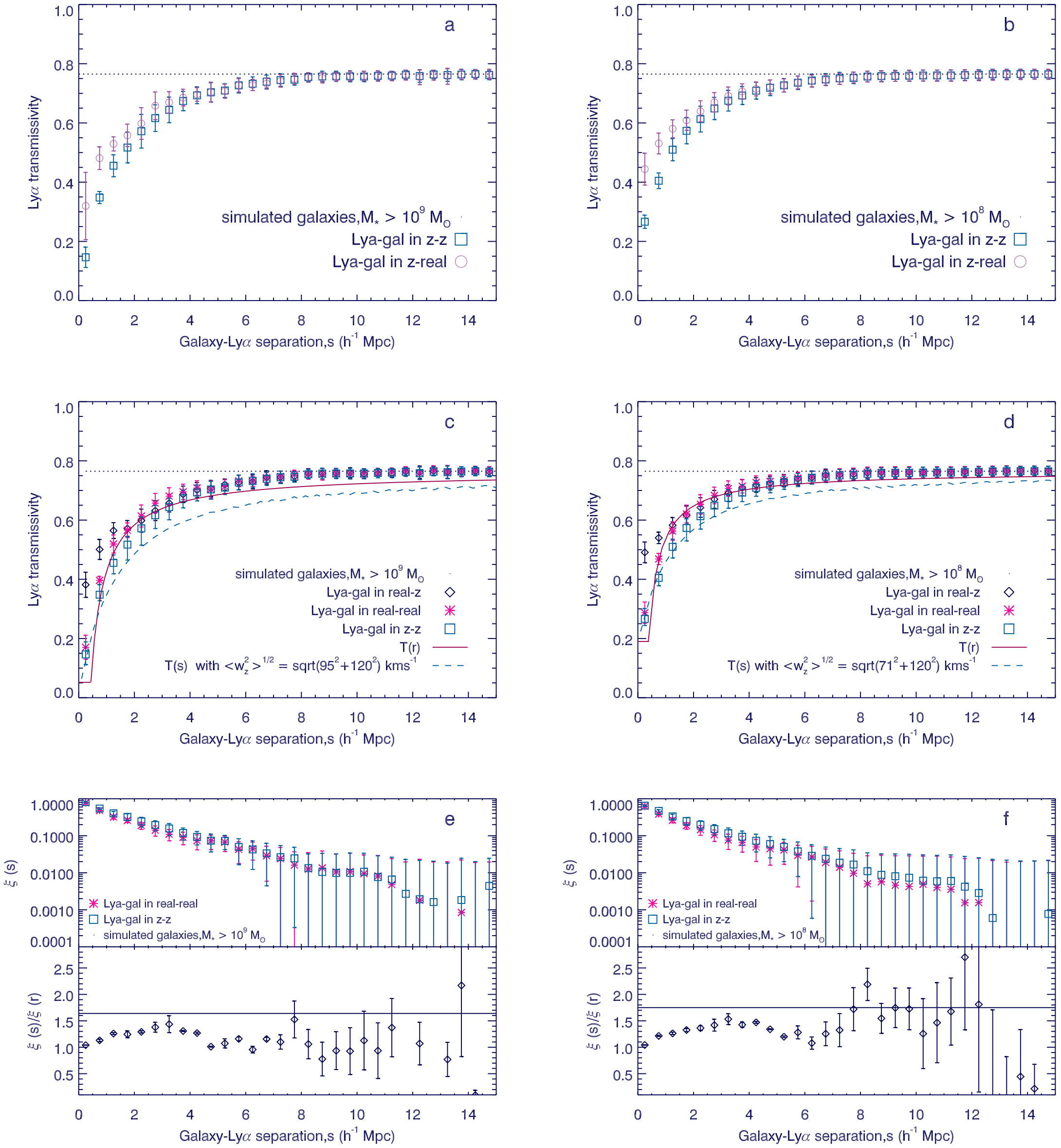

Figure 10. Lyα-galaxy transmissivity, $\langle T(s)\rangle$ from GIMIC $M_\star \geqslant 10^9$ $\mathrm{M}_\odot$ and $M_\star \geqslant 10^8$ $\mathrm{M}_\odot$ galaxy samples. The error bars are calculated by using jack-knife method. (a) $M_\star \geqslant 10^9$ $\mathrm{M}_\odot$ galaxy sample with $z-$space galaxies + $z-$space gas (light blue squares) and real-space galaxies + $z-$space gas (purple circles). (b) Same as (a) for $M_\star \geqslant 10^8$ $\mathrm{M}_\odot$ galaxies. (c) Lyα-galaxy transmissivity for $M_\star \geqslant 10^9$ $\mathrm{M}_\odot$ sample with Lyα-galaxies in real-z (blue diamonds), real-real (pink asterisks) and in $z-z$ (light blue squares). A fit to the real-real $\xi(r)$ with $r_0 = 0.30$ h^{-1} Mpc, $\gamma = 0.90$ is shown (red line). The expected Lyα-galaxy $\xi(s)$ in $z-z$ space with $\beta_{Ly\alpha} = 1.3$,$\beta_{gal} = 0.35$ and $\langle w_z^2\rangle^{1/2} = \sqrt{95^2+120^2}$ kms^{-1} is also shown (light blue dashed line). Note that these velocities are calculated from pairs within $s < 1$ h^{-1}Mpc. (d) Same as (c) for the $M_\star \geqslant 10^8$ $\mathrm{M}_\odot$ galaxy sample. Here the $\xi(r)$ fit assumes $r_0 = 0.21$ h^{-1} Mpc, $\gamma = 0.95$ and the $\xi(s)$ model assumes $\beta_{Ly\alpha} = 1.3$,$\beta_{gal} = 0.53$ and $\langle w_z^2\rangle^{1/2} = \sqrt{71^2+120^2}$ kms^{-1}. (e) $\xi(s)$ and $\xi(s)/\xi(r)$ for the high mass galaxy sample. The blue line in the lower panel represents the linear theory prediction with $\beta_{gal} = 0.35$, $\beta_{Ly\alpha} = 1.3$ giving $\xi(s)/\xi(r) = 1.64$. (f) Same as (e) for the $M_\star \geqslant 10^8$ $\mathrm{M}_\odot$ galaxy sample with $\beta_{gal} = 0.53$, $\beta_{Ly\alpha} = 1.3$ giving $\xi(s)/\xi(r) = 1.75$.

using $\xi(r) = \left(\frac{r}{r_0}\right)^{-\gamma}$ with $r_0 = 0.30$ h^{-1} Mpc, $\gamma = 0.90$ for $M_\star \geqslant 10^9$ $\mathrm{M}_\odot$ galaxies and $r_0 = 0.21$ h^{-1} Mpc, $\gamma = 0.95$ for $M_\star \geqslant 10^8$ $\mathrm{M}_\odot$ galaxies. Taking into account a Kaiser boost of $\xi(s)/\xi(r) \approx 1.5$, this r_0 for the high mass sample is reasonably consistent with the s_0 =0.3 h^{-1} Mpc fitted to the GIMIC cross-correlation $\xi(s)$ in Fig. 10 (see also Crighton et al. 2011). Thus the pink lines in Fig. 10 (c and d) represent $T(r) = \bar{T} - (\frac{r}{r_0})^{-\gamma}$. $\bar{T}$ is the mean Lyα transmissivity at $z \approx 3$ (A05).

We then apply the linear theory redshift-space distortion model of Kaiser (1987), in the form for cross-correlation $\xi(s)/\xi(r) = (1 + \frac{1}{3}(\beta_{gal} + \beta_{Ly\alpha}) + \frac{1}{5}\beta_{gal}\beta_{Ly\alpha})$ discussed by Mountrichas & Shanks (2007). As indicated earlier we shall assume the value $\beta_{Ly\alpha} = 1.3$ to represent the $1.0 < \beta < 1.6$ range suggested from the simulations of McDonald (2003).

The z-space distortion analysis is then implemented following da Ângela et al. (2008). Focussing again on the $M_\star \geqslant 10^8$ M$_\odot$ galaxies sample, we assume the appropriate values above of r_0 and γ, with dynamical infall values $\beta_{gal} = 0.53$ and $\beta_{Ly\alpha} = 1.3$, predicting $\xi(s) = 1.75 \times \xi(r)$, plus velocity dispersion $\sqrt{(173/\sqrt{2})^2 + 120^2} = 171$ kms^{-1}. This provides a poor fit even when we reduce the galaxy velocity dispersion from 122 kms^{-1} to 71 kms^{-1}, previously suggested to be the 'within-clump' value (see Fig. 10 (d, f)). It is the $\beta_{Ly\alpha} = 1.3$ value that is proving too high here, resulting in this model tending to over-predict the Lyα-galaxy cross-correlation function. The $M_\star \geqslant 10^8$ M$_\odot$ galaxy sample rather indicates in (f) that $\xi(s) \approx 1.4 \times \xi(r)$ implying $\beta_{Ly\alpha} \approx 0.7$. Similar results are found for the high mass sample of $M_\star \geqslant 10^9$ M$_\odot$ galaxies (see Fig. 10 (c,e)) where fits in (e) indicate $\beta_{Ly\alpha} \approx 0.15$.

The GIMIC Lyα-LBG $\xi(\sigma, \pi)$ results are presented in Fig. 11(a,b,c,d). Panels (a) and (b) show the Lyα-LBG result from $M_\star \geqslant 10^9$ M$_\odot$ galaxies in $r - r$ and $z - z$ respectively while panels (c) and (d) present the Lyα-LBG result from $M_\star \geqslant 10^8$ M$_\odot$ galaxies. Panels (e) and (f) give the $\langle w_z^2 \rangle^{1/2}$ versus β $\Delta\chi^2$ contours for GIMIC Lyα-LBG $\xi(\sigma, \pi)$ with $M_\star \geqslant 10^9$ M$_\odot$ galaxies and panels (g) and (h) the same for the $M_\star \geqslant 10^8$ M$_\odot$ galaxy sample. For the models we have assumed the same values of r_0, γ and (in the $z - z$ case) β_{gal} as above. We again note that we see little change in the shape of $\xi(\sigma, \pi)$ between the $r - r$ and $z - z$ results, suggesting that the effect of the peculiar motions, apart from coherent bulk motion, is again small. Restricting the fitting range to $\sigma, \pi < 12$ h^{-1}Mpc we find a fit to the $r - r$ $\xi(\sigma, \pi)$ giving $\beta_{Ly\alpha} = 0.02$ and $\langle w_z^2 \rangle^{1/2} = 20$ kms^{-1}, with reduced $\chi^2 = 1.2$. Fitting to the $z - z$ correlation function gives $\beta_{Ly\alpha} = 0.15$ and $\langle w_z^2 \rangle^{1/2} = 40$ kms^{-1}, with reduced $\chi^2 = 1.8$. Panels (g) and (h) show equivalent contour plots to panels (e) and (f) but with $M_\star \geqslant 10^8$ M$_\odot$ galaxies. The best fit for $r - r$ gives $\beta_{Ly\alpha} = 0.55$, $\langle w_z^2 \rangle^{1/2} = 60$ kms^{-1}, and reduced $\chi^2 = 0.6$, assuming $r_0 = 0.21$ h^{-1}Mpc and $\gamma = 0.95$. The best fit for $z - z$ gives $\beta_{Ly\alpha} = 0.7$, $\langle w_z^2 \rangle^{1/2} = 60$ kms^{-1}, and reduced $\chi^2 = 0.8$.

For the $M_\star \geqslant 10^8$ M$_\odot$ galaxies, the values that we would expect are $\beta = \langle w_z^2 \rangle^{1/2} = 0$ for the $r - r$ case and $\beta_{Ly\alpha} = 1.3$ and $\langle w_z^2 \rangle^{1/2} \approx \sqrt{120^2 + 71^2} = 139$ kms^{-1} for the $z - z$ case. From the $\Delta\chi^2$ contours in Fig. 11 we see that in the $z - z$ cases such values are quite clearly rejected by the simulated data, the more so when it is realised that the best fit parameters for both mass ranges are the same in $z - z$ and in $r - r$. We conclude again that the main result is the lack of difference between the real and redshift space fits for both high and low mass galaxies. We conclude that the effect of peculiar motions on the simulated $z - z$ 2-D correlation function is smaller than expected both for the gas infall parameter and for the gas-galaxy velocity dispersion. The explanation may be due the gas motion being coherent with the galaxies and so $\langle w_z^2 \rangle^{1/2} \approx 120$kms^{-1} may need reducing to $\langle w_z^2 \rangle^{1/2} \approx 71$kms^{-1} as for the galaxies implying $\langle w_z^2 \rangle^{1/2} \approx 100$kms^{-1} which is less easy to reject at least in the case of the low mass galaxies in (h).

5.2.3 Simulation and observation compared

We next compare the simulated results for Lyα-galaxy $\xi(s)$ with the Keck+VLRS data as shown in Fig. 8. The Keck + VLRS result shown is the full sample including A03, A05 and VLRS rather than VLRS plus the 6 re-reduced Keck QSOs because the larger number of QSOs means that the errors are smaller at $s < 1$ h^{-1}Mpc. The pink dot-dashed line shows the GIMIC $z - z$ space result. We have assumed the same model as Crighton et al to fit the GIMIC result ie $\langle T(s) \rangle = \bar{T} - (s/s_0)^{-1}$ with $s_0 = 0.3$ h^{-1}Mpc with a small-scale cutoff with $T = 0.29$ for $s < 0.5$ h^{-1} Mpc. The blue solid line is the expected Lyα-Galaxy $\xi(s)$ when convolving the empirically determined velocity errors of $\langle w_z^2 \rangle^{1/2} = \sqrt{(420^2 - 2 \times 100^2)/2} = 280$ kms^{-1} into this. Our bin size is 0.5 h^{-1}Mpc. The GIMIC model convolved with the empirical velocity dispersion lies above the LBG-Lyα data but only at the $1 - 2\sigma$ level and we regard it as being in excellent agreement with the combined LBG-Lyα data.

We finally compare the simulated results for Lyα-galaxy $\xi(\sigma, \pi)$ now with the 6 Keck QSOs + VLRS data as shown in Fig. 9. We have seen that the observed best fit parameters for the Keck + VLRS data are $\beta_{Ly\alpha} = 0.02$, $\langle w_z^2 \rangle^{1/2} = 100$ kms^{-1} and we noted that the measured infall parameter of $\beta_{Ly\alpha} = 0.02$ was $\approx 3\sigma$ lower than the expected value of $\beta_{Ly\alpha} = 1.3$. The best fit parameters for the simulated $M_\star \geqslant 10^8$ M$_\odot$ galaxy sample are $\beta_{Ly\alpha} = 0.70$, $\langle w_z^2 \rangle^{1/2} = 60$ kms^{-1}. This simulated $\beta_{Ly\alpha}$ value therefore lies between the expected value of $\beta_{Ly\alpha} = 1.3$ and the observed Keck+VLRS value of $\beta_{Ly\alpha} = 0.02$, an intermediate result where the $\Delta\chi^2$ contours shown in panel b of Fig. 9 allow consistency with both these values. We conclude the Keck+VLRS data also prefers low values of $\beta_{Ly\alpha}$ like the simulation. We also note that neither the minimum value of $\langle w_z^2 \rangle^{1/2} = 297$ kms^{-1} from LBG velocity error nor the $\langle w_z^2 \rangle^{1/2} = 320$ kms^{-1} value from including the full simulated $\langle w_z^2 \rangle^{1/2} = 120$ kms^{-1} is consistent with the data at the few sigma level. We conclude that while the Keck+VLRS $\beta_{Ly\alpha}$ and $\langle w_z^2 \rangle^{1/2}$ estimates are low compared to initial expectation from theory, they may still be consistent with the similarly low values of these parameters estimated from $\xi(s)$ and $\xi(\sigma, \pi)$ in the simulations.

5.3 Lyα auto-correlation

We measure the Lyα auto-correlation along and across QSO lines-of-sight. By doing this, we can measure the velocity dispersion of Hi gas to see if this has a significant effect on the Lyα-LBG cross-correlation function. Following Crighton et al. (2011), for each pixel in a QSO line-of-sight, we calculate

$$\delta = \frac{T}{\bar{T}} - 1 \qquad (7)$$

where T and $\bar{T}$ are the measure and the mean transmissivity. We used this to calculate the correlation

$$\xi(\Delta r) = \langle \delta(r) \delta(r + \Delta r) \rangle \qquad (8)$$

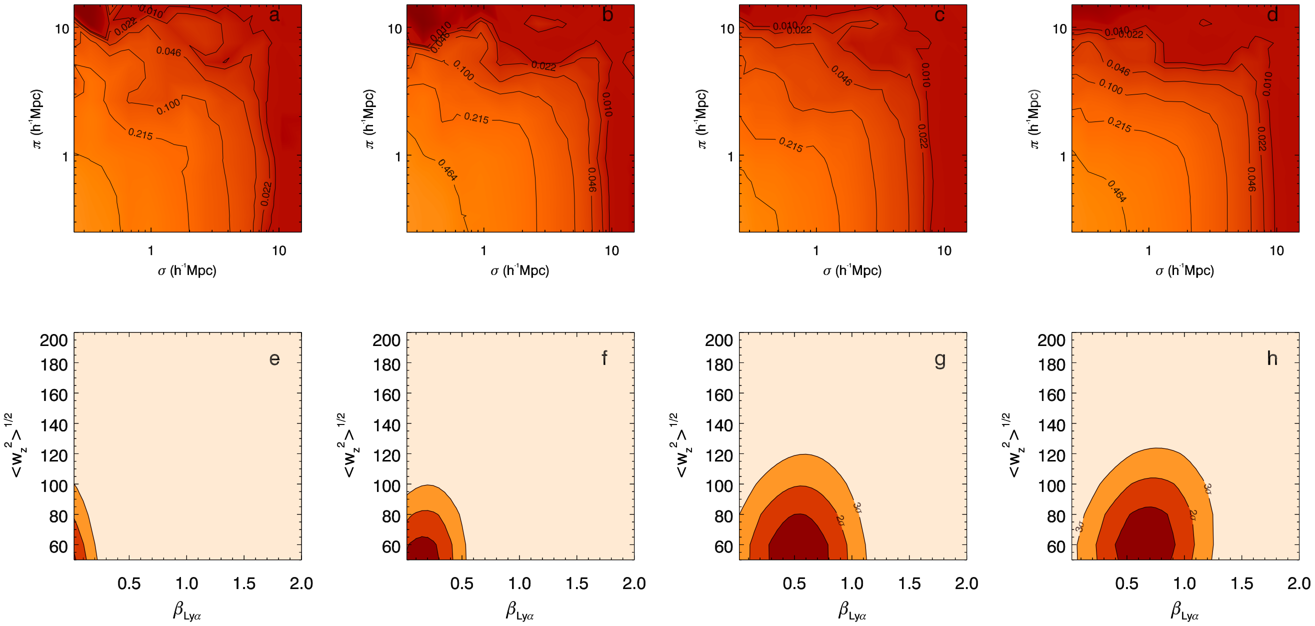

Figure 11. The top row shows the GIMIC Lyα-galaxy $\xi(\sigma,\pi)$ from $M_\star \geqslant 10^9$ M$_\odot$ (a,b) and $M_\star \geqslant 10^8$ M$_\odot$ galaxy samples (c,d) and in real-real space (a,c) and in $z-z$ space (b,d). The errors were calculated by using the jack-knife method. The bottom row shows the pairwise velocity dispersion ($\langle w_z^2\rangle^{1/2}$)-infall parameter($\beta_{Ly\alpha}$) $\Delta\chi^2$ contours for GIMIC Lyα-LBG $\xi(\sigma,\pi)$ fits in the range $s < 12\,h^{-1}$Mpc. (e) The best fit for real-real $M_\star \geqslant 10^9$ M$_\odot$ sample is $\beta_{Ly\alpha} = 0.02$, $\langle w_z^2\rangle^{1/2} = 20$ kms^{-1}, assuming $r_0 = 0.3\ h^{-1}$Mpc and $\gamma = 0.9$. (f) The best fit for $z-z$ $M_\star \geqslant 10^9$ M$_\odot$ sample is $\beta_{Ly\alpha} = 0.15$, $\langle w_z^2\rangle^{1/2} = 40$ kms^{-1}. (g) The best fit for real-real $M_\star \geqslant 10^8$ M$_\odot$ sample is $\beta_{Ly\alpha} = 0.55$, $\langle w_z^2\rangle^{1/2} = 60$ kms^{-1}, assuming $r_0 = 0.21\ h^{-1}$Mpc and $\gamma = 0.95$. The best fit for $z-z$ $M_\star \geqslant 10^8$ M$_\odot$ sample is $\beta_{Ly\alpha} = 0.70$, $\langle w_z^2\rangle^{1/2} = 60$ kms^{-1}.

We sum all pixels with the separations Δr, both parallel and perpendicular to r. We repeat this process for the QSO data listed in Table 1 and for the simulations.

Fig. 12 (a) shows the auto-correlation of Lyα pixels along the line-of-sight from the observational data. Keck, VLRS and combined samples are presented by pink diamonds, light blue asterisks and blue circles respectively. Error bars were estimated by using jack-knife method. We first compare these to the result from Crighton et al. 2011 (triangles) who measured the auto-correlation using 7 high resolution QSOs (resolution FWHM $\sim$ 7 kms^{-1}). The agreement appears to be excellent.They all show similar results at small scales. We also compared our results with the recent BOSS result of Slosar et al. 2011 (squares) but it is mostly seen at large scales as they are more interested in large-scale correlations.

The auto-correlation of simulated Lyα pixels are presented in Fig. 12 (b). The real and redshift-space Lyα auto-correlations are shown as the asterisks and diamonds, respectively. The real-space gas simulations are derived from the redshift-space simulations by switching off the effect of peculiar velocities in the output data. We then compare these to the result from Keck+VLRS. They show a good agreement.

Focussing on the simulation, we see again that the redshift and real-space correlation functions are quite similar in amplitude and form. At small scales, convolving the real-space correlation function with a Gaussian of width $120 \times \sqrt{2} = 170$ kms^{-1} representing the simulation gas peculiar velocity (see Fig. 2) is seen to overestimate the small-scale turnover in the redshift-space correlation function. This is better fitted by a velocity dispersion of width 30 kms^{-1} but this assumes $\beta_{Ly\alpha} = 0$ which is unphysical. Now at larger scales we see that the observed ratio of $\xi_s/\xi_r \approx 1.5$ is smaller than that expected from the linear theory in Equation 3. For the gas the value of the bias is $b \approx 0.3$ which arises from comparing the mass linear correlation function to the simulated real-space correlation function in Fig. 12 in the range $1 < r < 6\ h^{-1}$Mpc. This bias corresponds to $\beta_{Ly\alpha} \approx 3.3$ which implies $\xi(s)/\xi(r) \approx 5.4$. But again as noted by McDonald (2003), $\beta_{Ly\alpha}$ has no simple relation to density bias as for galaxies. $\beta_{Ly\alpha}$ has to be estimated from simulations and the simulations of McDonald et al implied a range $\beta_{Ly\alpha} = 1-1.6$. If we therefore take $\beta_{Ly\alpha} = 1.3$, then this predicts $\xi(s)/\xi(r) = 2.2$ from Equation 3 whereas the simulated value in Fig. 12 is more like $\xi(s)/\xi(r) = 1.5$ which corresponds to $\beta \approx 0.7$. The reason for this discrepancy is unclear. With $\beta_{Ly\alpha} = 0.7$, the best fit velocity dispersion is $\langle w_z^2\rangle^{1/2} = 70$ kms^{-1}. Models where we fixed $\beta_{Ly\alpha} = 1.3$ and took $\langle w_z^2\rangle^{1/2} = 170$ kms^{-1} as expected from Fig. 5 were also strongly rejected. With $\beta_{Ly\alpha} = 1.3$, again a best fit value of $\langle w_z^2\rangle^{1/2} = 70$ kms^{-1} was found although the model was still rejected in a chi-square test.

Whatever value of $\beta_{Ly\alpha}$ is chosen it appears that the fitted value of the velocity dispersion is much lower than measured in the simulation. However, as shown by Crighton et al. (2011), the intrinsic width of the Lyα lines convolved with the instrumental response of the spectro-

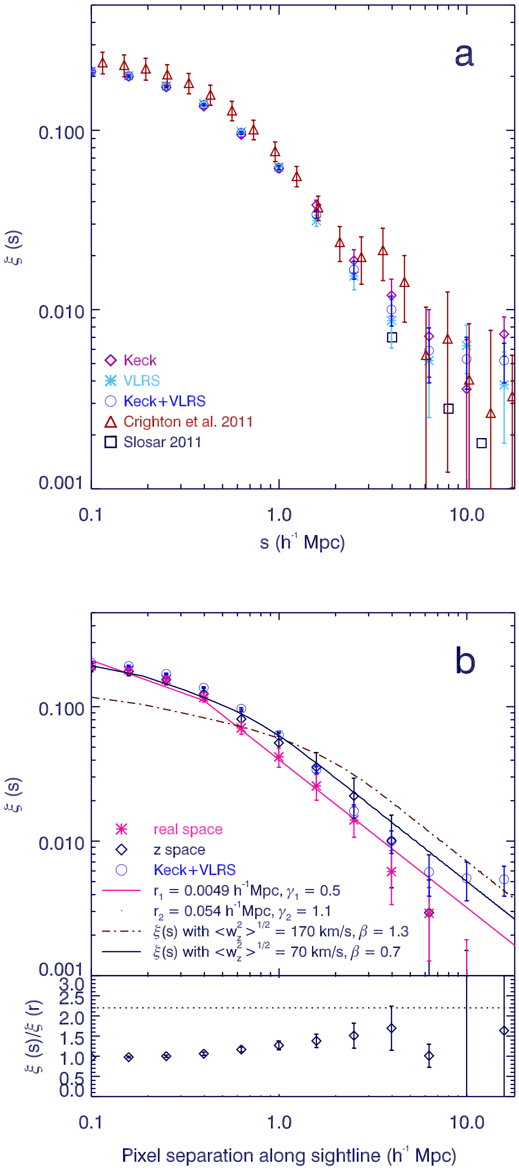

Figure 12. (a) The auto-correlation of Lyα pixels along the line-of-sight. Keck, VLRS and combined samples are shown by pink diamonds, light blue asterisks and blue circles respectively. The measurement of Crighton et al. (2011) is also shown (triangles). The recent BOSS result of Slosar et al. (2011) is also shown (squares). (b)-top panel : The auto-correlation functions of GIMIC Lyα pixels at $z = 3.06$ in the 0σ simulation. Real-space (pink asterisks) and $z - space$ (blue diamonds) results are shown. Errors are calculated via the jack-knife method. A double power-law fit to the real-space $\xi(r)$ with $r_{01} = 0.0049$, $\gamma_1 = 0.5$, $r_{02} = 0.054$, $\gamma_2 = 1.1$ is also shown (pink line). The brown dot-dashed line is the expected result for the Lyα $\xi(s)$ in z-space if we convolve in the velocity dispersion $\langle w_z^2 \rangle^{1/2} = 170$ kms^{-1} and $\beta_{Ly\alpha} = 1.3$ to the $z - space$ distortion model. The blue solid line is a predicted $\xi(s)$ with $\langle w_z^2 \rangle^{1/2} = 70$ kms^{-1}, $\beta_{Ly\alpha} = 0.7$ which appears to fit the simulated data. Bottom panel : GIMIC $\xi(s)/\xi(r)$ with jack-knife error bars. The dashed line corresponds to $\xi(s)/\xi(r) = 2.2$ as predicted from linear theory with $\beta_{Ly\alpha} = 1.3$.

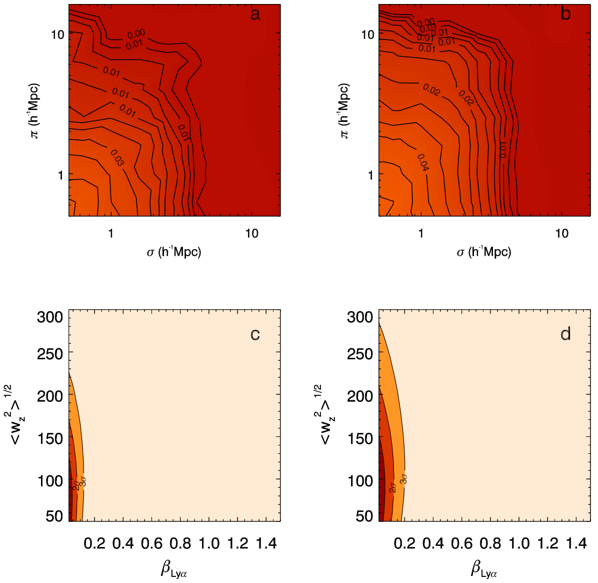

Figure 13. GIMIC Lyα $\xi(\sigma, \pi)$ at $z = 3.06$ in real and z-space. (a) Lyα real-space autocorrelation function. (b) Lyα z-space autocorrelation function. (c) Pairwise velocity dispersion ($\langle w_z^2 \rangle^{1/2}$)-infall parameter($\beta$) $\Delta\chi^2$ contours for GIMIC, fitting real-space $\xi(\sigma, \pi)$ in the range $s < 8$ h^{-1}Mpc. The best fit is $\beta = 0.02$, $\langle w_z^2 \rangle^{1/2} = 80$ kms^{-1} and reduced $\chi^2 = 1.1$, assuming $r_{01} = 0.0049$ h^{-1}Mpc , $r_{02} = 0.054$ h^{-1}Mpc ,$\gamma_1 = 0.5$, $\gamma_2 = 1.1$ and break point is at 0.40 h^{-1}Mpc. (d) As (c) for z-space. Here the best fit is $\beta = 0.02$, $\langle w_z^2 \rangle^{1/2} = 80$ kms^{-1} and $\chi^2 = 2.4$, assuming the same double power-law fit for $\xi(r)$.

graph can induce artificial autocorrelations at scales $\lesssim 0.7$ h^{-1}Mpc, so this effect may contribute to the poor fit of the peculiar velocity z-distortion model on small scales.

We note that the z-distortion model for the Ly-α auto- and cross-correlation assumes spherical symmetry as we move from real-space to redshift-space and the Lyα autocorrelation function involves summing along and across QSO lines of sight which may not be exactly spherically symmetric. However, we shall see that this explanation cannot apply to the Lyα $\xi(\sigma, \pi)$ which we calculate next and which gives consistent results.

For each pixel in the Lyα line-of-sight, we next calculate the Lyα $\xi(\sigma, \pi)$ by using,

$$\xi(\sigma, \pi) = \frac{\langle DT(\sigma, \pi) \rangle}{N(\sigma, \pi)} \tag{9}$$

where $< DT(\sigma, \pi) >$ is the number of Lyα pairs weighted by the normalized transmissivity: T_z, for each separations. N(σ, π) is the number of Lyα pixels that contributed to each pair.

The Lyα $\xi(\sigma, \pi)$ results at $z = 3.06$ for the 0σ simulation are shown in Fig. 13, the left hand side showing the result in real space and the right hand side showing the result in redshift-space. We see similar results for $r - r$ and $z - z$ space. Again there is little evidence of smoothing due to Gaussian convolution or flattening due to infall in Lyα autocorrelation. Thus the best fit model for $r - r$ is $\langle w_z^2 \rangle^{1/2} = 80$ kms^{-1}, $\beta_{Ly\alpha} = 0.02$. For $z - z$ the best fit parameters are the same, $\beta_{Ly\alpha} = 0.02$ and $\langle w_z^2 \rangle^{1/2} = 80$ kms^{-1}. The expected value of $\beta_{Ly\alpha} = 1.3$ is as strongly rejected for $z-z$ as for $r-r$ with $\chi^2_{red} = 11$). We again conclude that the effects of infall in the gas in the GIMIC simulation are much less than expected from the previous work of McDonald (2003) with an upper limit of $\beta_{Ly\alpha} = 0.7$ from $\xi(s)$ and $\beta_{Ly\alpha} \approx 0$ from Lyα $\xi(\sigma, \pi)$. Given $\beta = 0.7$, a gas velocity dispersion of $\langle w_z^2 \rangle^{1/2} = 70$ kms^{-1} fits the simulated Lyα $\xi(s)$ and this is close to the sub-1h^{-1}Mpc value of the velocity dispersion estimated for simulated galaxies, due to correlated motions. Good agreement is observed between the GIMIC simulation and the Keck+VLRS gas $\xi(s)$. We have not calculated the Lyα 2-D autocorrelation as the QSO sample does not have a high enough sky density to properly probe the on-sky projected profile.

6 DISCUSSION

A feature of this study is that we want to combine the power of the VLRS at large spatial scales with the statistical power of the Keck sample of A05 at smaller scales. Crighton et al. (2011) have included the Keck data in the LBG-Lyα cross-correlation function by simply using an error weighted combination of the Keck and VLRS correlation functions. Our aim here was to combine the two surveys for 2-D, $\xi(\sigma, \pi)$ correlation function analyses at the deeper level of the Lyα fluxes and LBG positions. We therefore included 940 $2.67 \leqslant z \leqslant 3.25$ LBGs from the Steidel et al. (2003) Keck samples. We also re-reduced 6 high resolution spectra of the QSOs in these fields from the ESO or Keck archives. With ≈ 3000 galaxies the combined VLRS and Keck surveys covering the widest wide range of spatial scales are ideal to study the dynamical relationship between galaxies and the IGM at $z \approx 3$.

The other new feature of this work is our use of the GIMIC simulations to help interpret the above correlation function results. The simulations are used to create synthetic Lyα spectra and galaxies. We study both galaxy clustering and the relationship between gas and galaxies via the auto- and cross-correlation functions in both 1-D and 2-D.

We first compared the simulated galaxy-galaxy results in real- and redshift-space. The LBG-LBG $\xi(r)$ and $\xi(s)$ in real and redshift space appear to be power laws at large scales. They show strong clustering at small separations. At small distances ($s < 1$ h^{-1} Mpc), the LBG-LBG $\xi(s)$ in redshift-space tends to have lower clustering than $\xi(r)$ in real space, while at larger scales the LBG-LBG $\xi(s)$ results appear to have higher clustering. Qualitatively this is as expected from 'finger-of-God' effects at sub 1 h^{-1}Mpc scales and dynamical infall at larger scales. Quantitatively, the large scale Kaiser boost for the galaxies is consistent with expectations. However, at smaller scales the peculiar velocity dispersion measured in the simulation overestimates the difference between real and z-space correlation functions. Similar results may have been found by Taruya et al. (2010) who found that at high redshift fitting finger-of-god damping terms, as we do here, tended to underestimate the peculiar velocity dispersion predicted by linear theory. Certainly, a 'local' velocity dispersion measured relative to galaxy pairs with separations < 1 h^{-1}Mpc produces improved agreement. For the galaxy $\xi(\sigma, \pi)$ there appears again to be little difference between the real-and z-space correlation functions but the results are still noisy. Clearly none of the correlation function statistics will pick up the most obvious indication of peculiar velocity in these simulated data which is the bulk motion of ≈ 100 kms^{-1} across the simulated volume. We will see that these unexpectedly small effects of peculiar velocity are also apparent as we move to study the gaseous component.

We then checked the LBG-Lyα transmissivity cross-correlation function as calculated directly from spectra and LBG positions of the Keck survey against the results of A03 and found good agreement, although we only had access to 6 out of their 8 QSO spectra. We checked the results for the combined Keck and VLRS surveys against the weighted combinations of Crighton et al. (2011) and again found good agreement. Our overall results for the Keck+VLRS LBG-Lyα $\xi(s)$ resemble more those of A05 and Rakic et al. (2012) than those of A03 ie a continuous decrease in Lyα transmissivity around the LBG with no evidence for a spike in transmissivity due to feedback being seen. Crighton et al. (2011) noted that such a spike could still be present but smoothed away by the errors in the LBG velocities.

The inclusion of the gas component along with the galaxies makes possible the search for gaseous infall. Assuming the appropriate dynamical infall parameter for the simulated $M_\star \geqslant 10^8$ M$_\odot$ galaxies, the gas- galaxy cross-correlation model gave $\beta_{Ly\alpha} \approx 0.7$, lower than the expected range of $1 < \beta_{Ly_\alpha} < 1.6$ from McDonald (2003). This small effect of the peculiar velocities was confirmed in the analysis of galaxy-Lyα $\xi(\sigma, \pi)$ where again the circular contours of the real-real $\xi(\sigma, \pi)$ was almost matched by those from the z-space version. Again there seems consistency with our view of a broadly coherent motion between gas and galaxies.

From the Lyα auto-correlations $\xi(s)$ and $\xi(\sigma, \pi)$, we see similar results with again small differences between real- and redshift-space. At small scales, the velocity dispersion needed to fit the simulated $\xi(s)$ is less than measured directly in the simulation, although this may be partly explained by the intrinsic width of the Lyα lines contributing artificial autocorrelation below separations of $\lesssim 0.7$ h^{-1}Mpc. At larger scales, the value of $\xi(s)/\xi(r)$ is more consistent with $\beta_{Ly\alpha} \approx 0.7 \pm 0.3$ rather than the range given by McDonald (2003), $\beta_{Ly\alpha} \approx 1 - 1.6$.

At larger scales, one possibility to explain the low gas infall rate may be due to the presence of feedback in the GIMIC simulations. Galaxy-wide winds of 600 kms^{-1} are invoked in the GIMIC simulations and this is a significant amount since this corresponds to 6 h^{-1}cMpc. These winds are modelled by each star particle that forms, imparting a randomly directed 600 kms^{-1} kick to 4 of its gas particle neighbours. It is possible that this outflow of the gas could cancel out some of the expected gravitational infall particularly in the neighbourhood of a galaxy. However, it remains to be seen whether enough gas particles are outflowing to explain the lack of infall in the gas cross- or auto-correlation functions. If the effects of gas outflow were detectable in the gas dynamics this could be a powerful probe, since there is not much evidence of feedback from any spike in transmission due to lower neutral gas density close to the galaxy.

7 CONCLUSIONS

We have analysed the interaction between IGM and galaxies at $z \sim 3$ using VLRS data and KECK LBGs, also the spectroscopy for 17 QSOs in the redshift range $2.5 < z < 4.0$ obtained from the publicly available QSO spectra and a spectrum from our own observations using the X-Shooter instrument on the VLT (Q2359+0653). Apart from the observational data, we employ the SPH GIMIC simulations to analyse the clustering of gas and galaxies.

1. The observed galaxy real space autocorrelation function is more consistent with that measured for simulated $M_\star \geqslant 10^9$ $\mathrm{M}_\odot$ galaxies than low mass galaxies. When an empirically determined velocity dispersion dominated by velocity errors is convolved with the simulated real space correlation functions, a similar preference is found for the lower amplitude clustering of the $M_\star \geqslant 10^9$ $\mathrm{M}_\odot$ galaxies. In the simulated data the difference between the real and redshift-space correlation functions is too small to be self-consistently explained by the measured peculiar velocity distribution. We suggest that this is the consequence of a scale dependence in the measurement of the peculiar motions and that the peculiar motions taken within $\lesssim 1\ h^{-1}$Mpc give a more consistent result.

2. We have checked for the existence of the transmission spike near star-forming galaxies in the data and GIMIC simulations which would be indicative of the effects of star-formation feedback on the IGM. For the data, we combined the full VLRS and Keck LBG-Lyα datasets to study both $\xi(s)$ and $\xi(\sigma,\pi)$ and the LBG-Lyα correlation functions. No detection of feedback is seen in the galaxy-gas correlation function in the VLRS+Keck data. We find that the gas transmissivity monotonically drops towards the galaxy, consistent with the density of neutral gas rising towards the galaxy position. Although the simulation transmission rises when LBG velocity errors are taken into account, the simulated and observational results remain in good statistical agreement.

3. The redshift-space gas-galaxy cross-correlation function in the simulation is close to the real-space correlation function and to some extent this is expected from linear theory applied to the Lyα forest flux which has a non-linear relation with optical depth and thus implies lower rates of dynamical infall of gas into galaxies than would otherwise apply. We have also considered whether galaxy-wide outflows may be cancelling out the infall effect.

4. The observed Lyα autocorrelation function is also consistent with the simulation. At small scales the difference between real and redshift-space correlation functions in the simulation is again less than expected given the peculiar velocity distribution but may be consistent with previous simulations of the Lyα forest. At larger scales the effects of dynamical infall are in line with linear theory, if the non-linear relation between flux and optical depth is taken into account. There may also be some residual effect from gas outflows cancelling out the effects of dynamical infall.

5. In the simulations, both gas and galaxies show evidence of a strong bulk motion. This bulk motion is undetectable by observable correlation functions but may have a connection with the local coherence needed to explain why distribution of peculiar velocities overestimates the finger-of-God effect.

ACKNOWLEDGEMENTS

We would like to thank Cai Yanchuan for the useful discussions. PT acknowledges financial support from the Royal Thai Government. TS and RMB would like to acknowledge the funding of their work through the UK STFC research grants. Simulations were performed on the ICC Cosmology Machine, which is part of the DiRAC Facility jointly funded by STFC, the Large Facilities Capital Fund of BIS, and Durham University.

REFERENCES

Adelberger K. L., Shapley A. E., Steidel C. C., Pettini M., Erb D. K., Reddy N. A., 2005, ApJ, 629, 636

Adelberger K. L., Steidel C. C., Shapley A. E., Pettini M., 2003, ApJ, 584, 45

Aguirre A., Schaye J., Hernquist L., Kay S., Springel V., Theuns T., 2005, ApJ, 620, L13

Bielby R., Hill M. D., Shanks T., Crighton N. H. M., Infante L., Bornancini C. G., Francke H., Héraudeau P., Lambas D. G., Metcalfe N., Minniti D., Padilla N., Theuns T., Tummuangpak P., Weilbacher P., 2013, MNRAS, 430, 425

Bielby R. M., Shanks T., Weilbacher P. M., Infante L., Crighton N. H. M., Bornancini C., Bouché N., Héraudeau P., Lambas D. G., Lowenthal J., Minniti D., Padilla N., Petitjean P., Theuns T., 2011, MNRAS, 414, 2

Cen R., Ostriker J. P., 1999, ApJ, 519, L109

Crain R. A., Theuns T., Dalla Vecchia C., Eke V. R., Frenk C. S., Jenkins A., Kay S. T., Peacock J. A., Pearce F. R., Schaye J., Springel V., Thomas P. A., White S. D. M., Wiersma R. P. C., 2009, MNRAS, 399, 1773

Crighton N. H. M., et al. 2011, MNRAS, 414, 28

da Ângela J., Outram P. J., Shanks T., Boyle B. J., Croom S. M., Loaring N. S., Miller L., Smith R. J., 2005, MNRAS, 360, 1040

da Ângela J., Shanks T., Croom S. M., Weilbacher P., Brunner R. J., Couch W. J., Miller L., Myers A. D., Nichol R. C., Pimbblet K. A., de Propris R., Richards G. T., Ross N. P., Schneider D. P., Wake D., 2008, MNRAS, 383, 565

Davis M., Efstathiou G., Frenk C. S., White S. D. M., 1985, ApJ, 292, 371

Dekel A., Birnboim Y., Engel G., Freundlich J., Goerdt T., Mumcuoglu M., Neistein E., Pichon C., Teyssier R., Zinger E., 2009, Nature, 457, 451

Dolag K., Borgani S., Murante G., Springel V., 2009, MNRAS, 399, 497

Frenk C. S., Evrard A. E., White S. D. M., Summers F. J., 1996, ApJ, 472, 460

Hamilton A. J. S., 1992, ApJ, 385, L5

Hawkins E., Maddox S., Cole S., Lahav O., Madgwick D. S., Norberg P., Peacock J. A., Baldry I. K., Baugh C. M., Bland-Hawthorn J., Bridges T., Cannon R., Colless M., Collins C., Couch W., 2003, MNRAS, 346, 78

Kaiser N., 1987, MNRAS, 227, 1

McDonald P., 2003, ApJ, 585, 34

McDonald P., Miralda-Escudé J., Rauch M., Sargent W. L. W., Barlow T. A., Cen R., Ostriker J. P., 2000, ApJ, 543, 1

Mountrichas G., Shanks T., 2007, ArXiv e-prints

Navarro J. F., Hayashi E., Power C., Jenkins A. R., Frenk C. S., White S. D. M., Springel V., Stadel J., Quinn T. R., 2004, MNRAS, 349, 1039

Oppenheimer B. D., Davé R., 2006, MNRAS, 373, 1265

Pettini M., Shapley A. E., Steidel C. C., Cuby J.-G., Dickinson M., Moorwood A. F. M., Adelberger K. L., Giavalisco M., 2001, ApJ, 554, 981

Power C., Navarro J. F., Jenkins A., Frenk C. S., White S. D. M., Springel V., Stadel J., Quinn T., 2003, MNRAS, 338, 14

Rakic O., Schaye J., Steidel C. C., Rudie G. C., 2012, ApJ, 751, 94

Rudie G. C., Steidel C. C., Trainor R. F., Rakic O., Bogosavljević M., Pettini M., Reddy N., Shapley A. E., Erb D. K., Law D. R., 2012, ApJ, 750, 67

Scannapieco C., et al. 2012, MNRAS, 423, 1726

Schaye J., Dalla Vecchia C., Booth C. M., Wiersma R. P. C., Theuns T., Haas M. R., Bertone S., Duffy A. R., McCarthy I. G., van de Voort F., 2010, MNRAS, 402, 1536

Shapley A. E., Steidel C. C., Erb D. K., Reddy N. A., Adelberger K. L., Pettini M., Barmby P., Huang J., 2005, ApJ, 626, 698

Shapley A. E., Steidel C. C., Pettini M., Adelberger K. L., 2003, ApJ, 588, 65

Slosar A., et al. 2011, JCAP, 9, 1

Springel V., 2005, MNRAS, 364, 1105

Springel V., Hernquist L., 2003, MNRAS, 339, 289

Springel V., White S. D. M., Tormen G., Kauffmann G., 2001, MNRAS, 328, 726

Steidel C. C., Adelberger K. L., Shapley A. E., Pettini M., Dickinson M., Giavalisco M., 2003, ApJ, 592, 728

Steidel C. C., Erb D. K., Shapley A. E., Pettini M., Reddy N., Bogosavljević M., Rudie G. C., Rakic O., 2010, ApJ, 717, 289

Taruya A., Nishimichi T., Saito S., 2010, Phys. Rev. D, 82, 063522

Theuns T., Leonard A., Efstathiou G., Pearce F. R., Thomas P. A., 1998, MNRAS, 301, 478

Theuns T., Viel M., Kay S., Schaye J., Carswell R. F., Tzanavaris P., 2002, ApJ, 578, L5

Weil M. L., Eke V. R., Efstathiou G., 1998, MNRAS, 300, 773

White S. D. M., Frenk C. S., 1991, ApJ, 379, 52

White S. D. M., Rees M. J., 1978, MNRAS, 183, 341